Enhancing the biocorrosion resistance and biocompatibility of Aluminium substrates using Graphene Oxide-PEDOT:PSS Hybrid Coating

*Sourya Subhra Nasker[1], Ragnhild Elizabeth Aune[2], Amogh K. Ravi[3], Tharangattu N. Narayanan[3], and Sasmita Nayak[1,4]**

[1]School of Biotechnology, Kalinga Institute of Industrial Technology (KIIT), Bhubaneswar, Odisha 751024, India
[2]Department of Materials Science and Engineering, Norwegian University of Science and Technology (NTNU), 7491 Trondheim, Norway
[3]Materials and Interface Engineering Laboratory, Tata Institute of Fundamental Research (TIFR), Hyderabad 500046, India
[4]Department of Microbiology, Kalinga Institute of Medical Sciences, Kalinga Institute of Industrial Technology Deemed to be University, Bhubaneswar, Odisha 751024, India

**Address all correspondence to Dr. Sasmita Nayak; E-mail: sasmita.n@kiitbiotech.ac.in*

Abstract

In the quest for advanced materials that can effectively combat biofilm-associated infections while ensuring material integrity, graphene oxide coated-aluminum (Al_GO) substrates have emerged as an innovative solution. Despite the well-documented antimicrobial capabilities of graphene oxide, its application at lower concentrations to preserve the structural and biological compatibility of metal alloys remains inadequately explored. This research addresses this gap by optimizing GO coatings at lower concentrations to achieve a delicate balance between antimicrobial efficacy and material biocompatibility. We explore the synergistic combination of electrochemically deposited GO at various concentrations (50, 100, 250, and 500 µg/mL) with PEDOT:PSS on AA1050 aluminum alloy (Al_GO/P). This approach aims to create a robust coating that enhances corrosion resistance, biocompatibility, and the antifouling properties of AA1050 Al, towards biofilm-forming organisms such as *Candida albicans*, *Staphylococcus aureus*, and *Escherichia coli*. Current study identifies that concentrations, particularly 100 and 250 µg/mL of GO on AA1050 aluminum alloy exhibit potent biocidal activity, while preserving aforementioned material properties. Since Al is an infinitely recyclable, green material, this work offers a sustainable alternative to traditional antimicrobial

surfaces. Further, this presents a contemporary strategy for surface modification of implantable biomedical devices, potentially reducing periprosthetic infection and extending device longevity; as well as for *ex vivo* material applications requiring strong antimicrobial performance.

Keywords: *Biocorrosion resistance; Microbiologically Influenced Corrosion (MIC); Antifouling properties; GO-PEDOT:PSS Coatings; Aluminium Alloy 1050; Biocompatibility.*

1. Introduction

Biofilms, structured microbial communities embedded within a self-produced extracellular matrix (ECM), pose a persistent clinical challenge due to their resilience to conventional therapies and impact on human health[1]. The ECM, also referred to as extracellular polymeric substances (EPS), not only supports nutrient absorption but also enhances microbial defense mechanisms against both host immune system responses and antimicrobial drugs[2]. Biofilm formation on medical devices such as implants, catheters, and ventilators often leads to chronic infections, which reduce the therapeutic effectiveness of interventions against medical device-associated infections (MDAIs). These infections significantly contribute to healthcare-associated infections (HAIs), a critical public health concern that affects approximately one in 31 hospitalized patients each day[3]. HAIs extend hospitalization periods, increase healthcare costs and are predominantly linked to invasive medical devices[3,4]. According to the European Center for Disease Prevention and Control (ECDC), the European Union and European Economic Area (EU/EEA) report over 4.3 million HAI cases annually, resulting in more than 90,000 deaths, exceeding the mortality burden of both influenza and tuberculosis in the region[5–7]. HAIs are also prevalent in the United States, where multidrug-resistant (MDR) infections contribute substantially to high morbidity and mortality rates[8–10]. In India, the burden is particularly severe, with HAI incidence ranging between 11% and 83% depending

on the infection type, underscoring systemic vulnerabilities in the healthcare infrastructure[11–15].

Previous research demonstrates that MDAI are typically caused by biofilms comprising mixed microbial communities, including Gram-negative bacteria (e.g., *Escherichia coli* and *Pseudomonas aeruginosa)*, Gram-positive bacteria (e.g., *Staphylococcus aureus*, *Staphylococcus epidermidis*, and *Enterococcus faecalis*), and fungi, predominantly the *Candida* species[16–18]. Microbial adhesion leads to biofouling, which subsequently initiates biocorrosion through the formation of differential aeration cells. These cells accelerate electrochemical degradation and pitting corrosion[19]. Unlike uniform corrosion, pitting results in severe, localized damage that compromises structural integrity and releases cytotoxic metal ions into the surrounding tissues[20]. The complex interplay between biofouling and biocorrosion highlights a key limitation of current implant materials, emphasizing the urgent need for surfaces engineered to resist both microbial colonization and corrosion-induced degradation[21,22].

These challenges reflect broader limitations to traditional implant materials, including stainless steel, aluminum, and synthetic polymers[23]. Their clinical use is often limited by cytotoxic effects, inflammatory host responses, and rapid degradation through either chemical or microbiologically influenced corrosion (MIC), often worsened by biofilm activity[24,25]. Metals and alloys such as 316L stainless steel, cobalt-chromium alloys, and titanium-based materials suffer from long-term performance issues arising from limited biocompatibility and corrosion-induced failure[26]. In chloride-rich physiological environments, mechanical wear and corrosion can release harmful ions such as cobalt, nickel, aluminum, and vanadium, raising significant concerns over systemic toxicity and neurotoxic effects[27,28]. Therefore, there is a clear need for advanced surface engineering strategies to develop materials that effectively mitigate biocorrosion and cytotoxicity without compromising performance[29].

Aluminum alloy AA1050 is widely used in multiple sectors due to its excellent thermal and electrical conductivity[30,31]. As a commercially pure alloy with a minimum aluminum content of 99.5%, AA1050 is particularly attractive for various applications including packaging, transportation, and electronics[32]. Its relatively lower density further enhances its suitability for aerospace and automotive components[30]. Although AA1050 demonstrates intrinsic corrosion resistance via the formation of a passive oxide layer under dry conditions, this protective barrier becomes compromised in humid or chloride-rich environments[33]. Under such conditions, AA1050 is vulnerable to MIC, as biofilms significantly alter the electrochemical landscape and promote corrosion [34].

To address these issues, recent advances in nanomaterials have facilitated the development of hybrid coatings that limit microbial adhesion and reduce the infection rates associated with devices[35]. Among these, the graphene family of materials (Gfam), especially graphene oxide (GO), has gained attention due to its high surface area, excellent barrier properties, strong adhesion to metals, and broad-spectrum antimicrobial properties[36–40]. When applied to AA1050 at a concentration of 1 mg/mL, GO forms a compact, impermeable barrier that effectively prevents the penetration of corrosive agents such as water, oxygen, and ions[41–44]. Moreover, the integration of the conductive polymer PEDOT:PSS with GO offers a synergistic advantage: GO-PEDOT:PSS hybrid coatings exhibit improved electrical conductivity[45], enhanced conductive pathways[46], and superior electron mobility[47]. Additionally, Singh *et. al.*[48] demonstrated that a GO-PIHA composite coating on copper significantly enhanced corrosion resistance[48].

Given the promising characteristics of the aluminum–graphene oxide-PEDOT:PSS (Al_GO/P) system, several key research questions arise: (1) How does the concentration of GO influence the antifouling efficacy of aluminum substrates against bacterial and fungal pathogens? (2) What GO concentration range provides the optimal balance between antibiofilm activity and

biocompatibility? (3) Does the aluminum GO/P system reduce biocorrosion relative to uncoated aluminum under simulated physiological conditions? Addressing these questions is essential for advancing healthcare-related applications through the strategic optimization of GO-PEDOT:PSS hybrid coatings on AA1050 substrates. Previous work from our laboratory demonstrated that GO coating concentrations in the range of 0.5–1.0 g/L exhibited strong antimicrobial activity but with limited biocompatibility[44]. Therefore, in this work, we evaluated the effect of lower concentrations of GO to achieve an optimal balance between antimicrobial efficacy and biocompatibility. Additionally, we incorporated a conductive polymer PEDOT:PSS at lower concentration (1 µg/mL) to enhance GO adhesion and reduce leaching while preserving the conductivity of the hybrid system. This approach was chosen to synergistically improve antimicrobial performance while minimizing cytotoxic effects.

In the present study, the antifouling performance, biocompatibility, and corrosion resistance of electrochemically deposited PEDOT:PSS polymer (1 µg/mL) integrated with GO at varying concentrations of 50, 100, 250, and 500 µg/mL on aluminum substrates, designated Al_GO50P, Al_GO100P, Al_GO250P, and Al_GO500P, have been evaluated. The modified surfaces were characterized using field emission scanning electron microscopy (FESEM) for GO distribution, Raman spectrophotometry for structural verification, four-point probe measurements for conductivity analysis, and assessments of surface hydrophobicity, adhesion strength, and porosity. The test pathogens, i.e., *Escherichia coli*, *Staphylococcus aureus*, and *Candida albicans*, were selected based on their clinical relevance to HAIs. Antibiofilm activity was assessed via fluorescence microscopy and crystal violet staining, focusing on polymicrobial *Candida*-bacterial biofilms. Mechanistic evaluations included the detection of intercellular reactive oxygen species (ROS) using fluorescent probes and analysis of microbial membrane disruption via SEM analysis. Corrosion rates were measured under both abiotic and biotic conditions according to ASTM standards[49]. Biocompatibility was confirmed through MTT

assays, supporting the potential use of these coatings in implantable medical devices, water purification systems, and industrial applications where biofilm mitigation is essential. The engineered Al_GO/P system thus represents a promising material alternative for improving both device longevity and patient outcomes across sectors.

2. Experimental Procedures

2.1. Substrates synthesis and characterization

2.1.1. Substrate preparation[44,48]

Aluminium plates (AA1050) with 99.5% purity and a thickness of 1.5 mm were obtained from NALCO India Ltd. The precursor graphene oxide (GO, 0.4 wt%) was purchased from Graphenea Inc., and poly(3,4-ethylenedioxythiophene): polystyrene sulfonate (PEDOT:PSS) was obtained from Sigma-Aldrich (Cat. no. #655201). For the experimental procedures, aluminum sheets were sectioned into 2.5 cm × 2.5 cm and 1.5 cm x 1.5 cm squares using an electric discharge machine (EDM) wire cutter. The aluminum substrates were then polished using silicon carbide emery papers of grit sizes ranging from P320 to P2000 to improve surface suitability for electrochemical deposition.

Subsequently, the substrates underwent ultrasonic cleaning in acetone [Cat. no. #31566, SRL] to eliminate any remaining polishing residues and were dried at room temperature.

A facile electrochemical deposition (ECD) process, involving optimization of an aqueous electrolyte, was used to coat the sterile aluminium substrate with a GO-PEDOT:PSS hybrid layer (Al_GO/P). The GO slurry was prepared by dispersing GO in 0.1 M sodium sulfate (Na_2SO_4) [Cat. no. #59977, SRL] to form a Na_2SO_4-GO suspension. The mixture was probe-sonicated for 1 hour to ensure uniform dispersion.

GO suspensions of 50 µg/mL, 100 µg/mL, 250 µg/mL, and 500 µg/mL were prepared. The pH of each suspension was adjusted to a neutral value of 7.0 by adding 0.1 M sodium hydroxide (NaOH) [Cat. no. #68151, SRL] dropwise under continuous stirring.

At this stage, prior to deposition, PEDOT:PSS was added to the GO suspension at a concentration of 1 µg/mL (25 µL).

Electrochemical deposition was carried out in a glass beaker using the cleaned aluminum sheet as the working electrode and a pure copper sheet as the counter electrode. A constant positive DC voltage of 30 V was applied using a Keithley 2601B source meter for 90 seconds to achieve a homogenous, uniform deposition.

Before proceeding to biological experiments, all bare and coated substrates were sterilized by autoclaving at 121°C under 15 lb pressure for 15 minutes, followed by ultraviolet light irradiation for 30 minutes to ensure sterility. Finally, all samples were washed twice with phosphate-buffered saline (PBS) and stored under sterile conditions until use.

2.1.2. Surface morphological analyses: Field emission scanning electron microscopy (FESEM)[44]

FESEM analysis was performed to assess the surface morphology and microstructural variations between the bare aluminum and Al_GO/P-coated substrates. Micrographs were obtained using a JSM-7200F Schottky FESEM (JEOL Ltd., TIFR Hyderabad Facility). The samples (2.5 cm × 2.5 cm) were placed in an ultrahigh vacuum chamber (10^{-6} mbar) and irradiated with high-energy electrons at an accelerating voltage of 5 kV.

To enhance surface conductivity and image resolution, samples were sputter-coated with a thin layer of gold prior to imaging. Observations were conducted using the secondary electron (SE) detection mode to obtain high-contrast micrographs of surface features.

2.1.3. Raman Spectrophotometry[50]

The structural identity of the GO layer in the Al_GO/P samples was characterized using a Renishaw inVia™ confocal Raman microscope. The Raman spectra were recorded at 25°C using a 532 nm laser as the excitation source. Spectral data were collected in the range of 101 cm^{-1} to 3202 cm^{-1} with a resolution of 0.8 cm^{-1}.

2.1.4. Water Contact Angle (WCA)[51]

The surface wettability of both bare aluminum and the Al_GO/P substrates was evaluated by measuring the static water contact angle (WCA) using a VCA Optima contact angle meter (AST Products Inc.). The sessile drop technique was employed, in which a droplet of ultrapure water was placed on the surface of each specimen. Images of the droplet were captured and analyzed to determine the contact angle, thereby indicating the relative hydrophobicity or hydrophilicity of the surface. The measurements were repeated at multiple points per sample to ensure reproducibility.

2.1.5. Four-probe conductivity measurement [52]

Bulk electrical conductivity of bare and Al_GO/P substrates was measured using the Van der Pauw method. A four-probe station and Keithley 2450 source meter (delta mode) were used for this purpose. Electrical contacts were placed at the edges of the substrate, and a 10 mA current was applied to measure the sheet resistance (R_s).

The bulk conductivity (σ) was calculated using the relation:

$$\sigma = \frac{1}{R_S t} \qquad \text{(Eq. 1)}$$

where t is the thickness of the aluminum substrate. All measurements were conducted under controlled ambient conditions, and the conductivity values were compared across different GO concentrations.

2.1.6. Porosity Evaluation [44,53–55]

The porosity of the hybrid coating was evaluated using electrochemical techniques in a 3.5 wt.% NaCl solution,[44,53–55] simulating a corrosive environment. A three-electrode setup was configured using a VSP-300 multichannel potentiostat/galvanostat (BioLogic, France). The working electrode was either a bare or coated aluminum substrate, the reference electrode was Ag/AgCl, and the counter electrode was a platinum mesh.

The active surface area was defined using an epoxy mask, exposing only 1 cm^2 of the sample. The open circuit potential (OCP) was monitored for 30 minutes until stabilization. Tafel polarization was carried out at a scan rate of 1 mV/s, over a potential range of ±250 mV relative to OCP at room temperature.

Tafel parameters, i.e., corrosion potential (E_{corr}) and anodic Tafel slope (β_a), were extracted using EC-Lab software.

Electrochemical impedance spectroscopy (EIS) was performed with an AC amplitude of 10 mV over a frequency range of 100 kHz to 100 mHz. Data fitting was carried out using equivalent circuit models to determine the polarization resistances (R_P) of both coated and uncoated samples.

The porosity P (%) was calculated using the following equation[56],

$$P = \left(\frac{R_{PS}}{R_P}\right) \times 10^{-\left(\frac{\Delta E_{corr}}{\beta_a}\right)} \qquad \text{(Eq. 2)}$$

where R_{PS} is the polarization resistance of the coated substrates, R_p the polarization resistance of the bare aluminum substrate, ΔE_{corr} the difference between the corrosion potential of the coated ($E_{corr,coatings}$) and bear ($E_{corr,A}$) substrates ($\Delta E_{corr}=E_{corr,coatings} - E_{corr,Al}$), and β_a the anodic Tafel slope of the bare aluminum.

224 **2.2. Antimicrobial and Antibiofilm Assay**

225 *2.2.1. Microbial cell culture*

226 *Candida albicans* (*C. albicans*) [fungus, ATCC 76485] cells were cultivated on Yeast-Peptone
227 Dextrose (YPD) agar [Cat. no. #G038, HiMedia] plates at 30°C for 24 hours. A single colony
228 was selected and inoculated into YPD broth [Cat. no. #M1363, HiMedia], which was then
229 incubated overnight at 25°C with shaking at 200 rpm. From this overnight culture, a secondary
230 culture was initiated at a 1:100 dilution and allowed to grow until it reached the mid-
231 logarithmic phase. The final fungal cell suspension was prepared to achieve a concentration of
232 10^8 CFU/mL.

233 *Escherichia coli* (*E. coli*) [Gram-negative bacterium, ATCC 29425] and *Staphylococcus aureus*
234 (*S. aureus*) [Gram-positive bacterium, ATCC 25923] cells were grown on Luria Bertani (LB)
235 agar [Cat. no. #G1151, HiMedia] plates at 37°C for 24 hours. A single colony was picked and
236 inoculated into LB broth [Cat. no. #G1245, HiMedia], followed by overnight incubation at
237 37°C with shaking at 200 rpm. From this culture, a secondary inoculum was prepared using a
238 1:100 dilution, which was then grown to the mid-logarithmic phase. The final bacterial cell
239 suspension was prepared to achieve concentrations of 10^7 CFU/mL and 10^8 CFU/mL,
240 depending on the assay.

241 For mixed *Candida*-bacterial biofilms, a suspension was prepared by mixing 1 mL each of the
242 *C. albicans*, *S. aureus*, and *E. coli* cultures in a 1:1:1 ratio [57].

243

244 *2.2.2. Microbial Growth Inhibition Assay*[50,58]

245 The Al_GO/P substrates (2.5 cm × 2.5 cm) were sterilized by autoclaving at 121°C for 15
246 minutes under 15 lb pressure, followed by ultraviolet light exposure for 30 minutes. 100 µL of

247 bacterial suspension containing 10^7 CFU/mL was pipetted onto different Al_GO/P and control
248 substrates (Glass and Bare Al) inside sterile Petri plates. These were incubated at 37°C for 2
249 hours under aseptic conditions.

250 After incubation, molten LB agar (45ºC) was poured over the substrates and allowed to solidify
251 at room temperature. The plates were then incubated overnight at 37°C, and bacterial colonies
252 were analyzed the following day.

253 Similarly, 100 µL of *C. albicans* suspension (10^7 CFU/mL) was incubated on distinct Al_GO/P
254 and control substrates in sterile Petri plates for 10 hours under aseptic conditions. Following
255 incubation, molten YPD agar (45ºC) was poured over the surfaces and allowed to solidify. The
256 plates were incubated overnight at 30°C, and fungal colonies were analyzed after 24 hours.

257 *2.2.3. Antibiofilm assay*[44]

258 A mixed microbial suspension was incubated on sterilized Al_GO/P substrates (150 µl/cm²)
259 placed in sterile Petri dishes at room temperature. To maintain constant humidity, the plates
260 were placed in closed containers containing autoclaved deionized water channels to prevent
261 desiccation stress.

262 The mixed suspension was seeded onto both control and Al_GO/P-coated substrates and
263 incubated for 10 hours. Two different inoculum concentrations (10^7 CFU/mL and 10^8 CFU/mL)
264 were tested in parallel to assess biofilm formation. After incubation, 100 µL of each residual
265 suspension was transferred to 35mm Petri plates containing a 1:1 mixture of YPD and LB
266 broth, supplemented with 10% fetal bovine serum (FBS) [Cat. no. # A5256901, Gibco], and
267 incubated at 37°C for an additional 10 hours.

268

269 *2.2.4. Fluorescence microscopy to visualize biofilm formation*

270 After 10 hours of incubation under biofilm-stimulating conditions (37°C with 10% FBS),
271 biofilm-coated substrates were gently washed with sterile distilled water to remove planktonic
272 cells. The remaining biofilm biomass was sequentially stained using dark conditions with:

273 • Calcofluor white [Cat. no. #18909, Sigma-Aldrich] for *C. albicans* (blue) [59–61]
274 • Acridine orange [Cat. no. #A9231, Sigma-Aldrich] for *S. aureus* (red)[62]
275 • Sodium fluorescein [Cat. no. #46960, Sigma-Aldrich] for *E. coli* (green)[63]

276 The dyes were prepared according to established protocols[63]. Fluorescence imaging was
277 performed using an EVOS Cell Imaging Station (Invitrogen) at 40× magnification.

278 *2.2.5. Biofilm biomass quantification*[64]

279 Following 10-hour incubation, 100 µL of each suspension was seeded into wells of a 96-well
280 plate containing YPD medium supplemented with 10% FBS and incubated at 37°C under static
281 conditions for an additional 10 hours.

282 The biofilms were washed three times with Milli-Q water to remove non-adherent cells. Then,
283 200 µL of 0.1% (w/v) crystal violet solution [Cat. no. #TC510, HiMedia] was added to each
284 well, and the plates were incubated at room temperature for 30 minutes on an orbital shaker at
285 70 rpm.

286 Excess stain was removed with three washes using Milli-Q water, and the wells were dried at
287 room temperature for 30 minutes. The retained stain was solubilized with 200 µL of 70% (v/v)
288 ethanol, and absorbance was measured at 595 nm.

289 • Growth control (GC): Glass substrate (100% biofilm)
290 • Sterility control (SC): Ultrapure water (0% biofilm)

291 Percentage biofilm growth was calculated using the following equation:

292 $$\% \, Biofilm \; growth = \frac{Sample_{A595} - SC_{A595}}{GC_{A595} - SC_{A595}} \; x \; 100 \qquad \text{(Eq.3)}$$

293 where $Sample_{A595}$ is the absorbance of the test substrate, SC_{A595} the absorbance of the sterility
294 control (0% biofilm), and GC_{A595} the absorbance of the growth control (100% biofilm).

295 *2.2.6. Detection of ROS production*[44,65]

296 Mixed *Candida*-bacterial suspension was seeded on sterile Al_GO/P substrates and incubated
297 at room temperature for 10 hours under constant humidity. 10 µM of 2',7'-
298 dichlorodihydroflourescein diacetate (H_2DCF-DA) [Cat. no. #D399, Invitrogen] was added to
299 the suspension and incubated for 20 minutes in the dark. Imaging was performed using an in-
300 house fluorescence microscope (Floid cell station, 40×, Invitrogen).

301 To detect surface-generated ROS, 10 µM of H_2DCF-DA was applied directly onto washed
302 substrates, and green fluorescence was recorded using a Nikon ECLIPSE Ci-E microscope at
303 40× magnification.

304 Mixed bacterial cell suspension was seeded on sterile Al_GO/P substrates and incubated at
305 room temperature for 10 hours under constant humidity. A 10 µM solution of the cytosolic
306 superoxide indicator dye dihydroethidium (DHE) [Cat. no. #D1168, Invitrogen] was used to
307 stain the suspension for 20 minutes in the dark[66]. Following incubation, cell imaging was
308 performed using an in-house fluorescence microscope (Floid Cell Station, 40×, Invitrogen).

309 To detect ROS generated at the material surface, a separate experiment was performed: mixed
310 bacterial cell suspension was seeded on sterile Al_GO/P substrates and incubated at room
311 temperature for 10 hours under constant humidity. After incubation, the substrates were rinsed
312 and placed under a fluorescence microscope. A 10 µM solution of DHE was then applied
313 directly to the surface of both the control and Al_GO/P substrates. The resulting red

fluorescence signal was captured using a Nikon ECLIPSE Ci-E microscope at 40× magnification.

2.2.7. Scanning electron microscopy (*SEM*)[44,50]

10^7 CFU of the mixed *Candida*-bacterial suspension were incubated over sterilized Al_GO/P substrates (150 µl/cm^2) placed in sterile Petri plates at room temperature for 10 hours under constant humidity. Following incubation, the cells were fixed with 2.5% glutaraldehyde and dehydrated through a graded ethanol series (30%, 60%, 70%, 80%, 90%), followed by treatment with 100% ethanol for 30 minutes.

The substrates were then sputter-coated with gold-palladium and imaged using a Gemini SEM 450 (Zeiss, KIIT Central Research Facility).

2.3. Evaluation of Corrosion Resistance

2.3.1. Description of immersion systems [34]

The experiments were carried out in two systems consisting of glass beakers with a usable volume of 300 mL, in which the substrates were fixed to the bottom after prior sterilization. The medium employed was a 1:1 mixture of LB and YPD broth, sterilized in an autoclave at 121°C and 15 lb pressure for 15 minutes. Both systems were assembled under aseptic conditions.

The abiotic system (control) contained only the sterile medium along with the following antibiotics: Fluconazole (antifungal, 15 µg/mL) [Cat. no. #22239, SRL], Chloramphenicol (antibacterial, 15 µg/mL) [Cat. no. #97686, SRL], and Vancomycin (antibacterial, 15 µg/mL) [Cat. no. #61078, SRL]. The biotic system included the same sterile medium, supplemented with 1% (v/v) of the mixed *Candida*-bacterial inoculum.

2.3.2. Weight loss measurement of the corroded substrates

After 45 days of exposure in both biotic and abiotic systems, weight loss was calculated following the chemical cleaning procedure described in ASTM G1-03 standard[49]. After removal of the biofilm, the samples were immersed in a 69.2 wt% nitric acid solution for approximately 5 minutes to remove corrosion products, rinsed with distilled water to eliminate residual acid, and then dried under flowing air.

The specimens were weighed before and after the experiment using an analytical balance, and the corrosion rate was calculated using the following equation:

$$Corrosion\ rate = \frac{(W\ x\ K)}{(A\ x\ T\ x\ D)}\ \mu mpy \qquad \text{(Eq. 4)}$$

where W is the weight loss, K the unit conversion constant (8.76 x10^7), A the exposed area, T the exposer time, D the material density, and μmpy the corrosion rate.

The measured corrosion rates were classified according to the NACE Standard RP-07-75[67], which provides validated guidelines for the preparation, analysis, and interpretation of corrosion measurements. All tests were performed in triplicate.

2.3.3. FESEM analysis of immersed Al_GO/P substrates

FESEM was used to investigate microstructural variations in the bare aluminum and the Al_GO/P substrates before and after 45-day immersion in both abiotic and biotic environments.

To observe the corrosion morphology, the substrates were cleaned in accordance with the ASTM G1-03 standard[49]. Micrographs were obtained using a JSM-7200F Schottky FESEM (JEOL Ltd., TIFR Hyderabad Facility), operated at an accelerating voltage of 30 kV. Samples of 2.5 cm × 2.5 cm were placed in an ultrahigh vacuum chamber (10^{-6} mbar). Prior to imaging, substrates were coated with a thin gold film to enhance surface conductivity and enable high-resolution image capture.

2.4. Cytotoxicity assay

360 *2.4.1. Mammalian Cell Culture* [68–71]

361 The Human Embryonic Kidney (HEK293T) cell line [ATCC CRL-11268] was used. HEK293T
362 is a well-established model and is widely employed in cytotoxicity assays, including the
363 evaluation of new biomaterials[72]. A frozen vial was retrieved from liquid nitrogen storage and
364 thawed using a standard defrosting protocol. The cells were cultured in Dulbecco's Modified
365 Eagle Medium (DMEM) [Cat. no. #10564011, Gibco] supplemented with 10% fetal bovine
366 serum (FBS) [Cat. no. # A5256901, Gibco] and 1X Antibiotic-Antimycotic solution [Cat. no.
367 #A002, HiMedia]).

368 Cells were maintained at 37°C in a humidified incubator with 5% CO_2 and 95% air. Upon
369 reaching approximately 80% confluency, biocompatibility experiments were initiated. Cell
370 counting was performed using a hemocytometer. Samples were prepared according to Sections
371 4.2 and 4.3 of ISO 10993-5: Biological Evaluation of Medical Devices - Part 5: Tests for In
372 Vitro Cytotoxicity, and the experiments were performed in compliance with Section 8 of the
373 same standard[73].

374 *2.4.2. Indirect (extract) assay*

375 HEK293T cells were seeded into 96-well plates at a density of $1x10^4$ cells per well and
376 incubated for 24 h. In parallel, extracts of the test materials were prepared. After sterilization
377 with 70% ethanol and ultraviolet light exposure for 30 minutes, the Al_GO/P substrates were
378 placed in 35 mm Petri plates containing fresh growth medium. The extraction procedure was
379 carried out at 37°C for 24 hours to obtain 100% crude extracts.

380 Once the seeded cells reached approximately 70% confluency, the culture medium was
381 replaced with the test extracts. Cells were incubated for an additional 24 and 48 hours. Each
382 condition was tested in triplicate.

383 Cell viability was assessed by incubating the cells in medium containing 0.5 mg/mL of 3-[4,5-
384 dimethylthiazol-2-yl]-2,5-diphenyltetrazolium bromide (MTT) [Cat. no. #CCK003, HiMedia]
385 for 2 hours. The medium was then replaced with isopropanol to solubilize the purple formazan
386 product, and absorbance was measured at 570 nm. Results are expressed as the percentage of
387 MTT signal relative to untreated control cells, which were defined as 100% viable.
388 Experiments were conducted according to Section 8.2 of ISO 10993-5: Biological Evaluation
389 of Medical Devices - Part 5: Tests for In Vitro Cytotoxicity[73].

390 *2.4.3. Direct contact assay*

391 HEK293T cells were seeded into 35 mm Petri plates and incubated for 24 and 48 hours in the
392 presence of pre-sterilized test samples (70% ethanol and ultraviolet light-treated), which were
393 carefully placed in the center of each plate. Each test material was evaluated in triplicate.

394 After incubation, cell viability was measured directly by adding 0.5 mg/mL MTT reagent to
395 the culture medium and incubating for 2 hours. The medium was then replaced with
396 isopropanol to extract the formazan dye, and absorbance was measured at 570 nm. Results
397 were reported as percentage MTT signal compared to the control, where untreated cells were
398 set at 100% viability. All procedures were carried out in compliance with Section 8.3 of ISO
399 10993-5: Biological Evaluation of Medical Devices - Part 5: Tests for In Vitro Cytotoxicity[73].

400

401

402

403

404

405

3. Results and Discussion

3.1. Material property assessment

3.1.1. Synthesis of Graphene oxide – PEDOT:PSS hybrid coated Aluminium (AA1050) substrates

The schematic diagram illustrating the facile two-step synthesis process for graphene oxide-coated Al substrates is presented in Figure 1. The inherent negative surface charge (zeta potential) of the aqueous GO dispersion causes anodic deposition at applied potentials of 10 volts or higher[44]. These electrostatic forces were sufficient to drive GO nanosheets toward the working electrode – the Al substrate[74]. As aforementioned, previous work from our lab showed that GO coatings at 0.5–1.0 g/L offered strong antimicrobial activity but poor biocompatibility, hence, we employed lower concentrations to balance antimicrobial activity vs biocompatibility[44]. Further, PEDOT:PSS was used at a reduced concentration (1 µg/mL) in the hybrid system to preserve conductivity while enhancing the adhesion of GO to the underneath metal. The sample preparation parameters for coating AA1050 substrates using GO (50, 100, 250, and 500 µg/mL) with PEDOT:PSS (1 µg/mL) is detailed in Table 1.

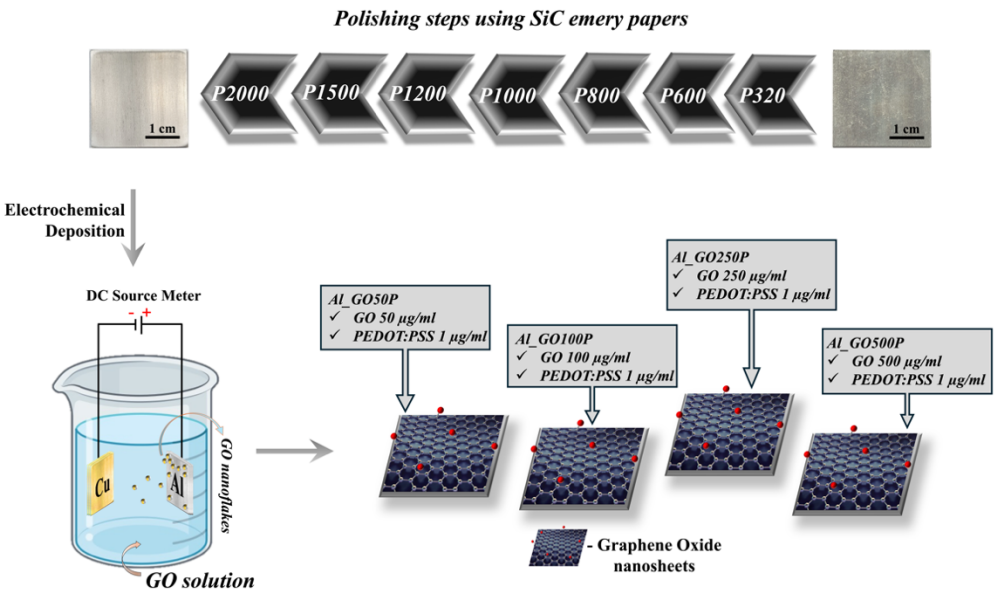

Figure 1. Facile two-step synthesis process of GO coated AA1050 substrates. Schematic diagram illustrating the preparation of Al_GO/P substrates, including sequential polishing of aluminum using SiC papers of varying grit sizes, followed by electrochemical deposition.

Table 1. The details of sample preparation parameters used for coating Al substrates using varied concentration of graphene oxide sourced from Graphenea Inc.

Sample Code	*GO concentration (in µg/mL)*	*PEDOT:PSS concentration (in µg/mL)*	*Voltage applied (in Volts)*	*Duration of deposition (in seconds)*
Al_GO50P	50	1	30	90
Al_GO100P	100	1	30	90
Al_GO250P	250	1	30	90
Al_GO500P	500	1	30	90

3.1.2. Raman Spectrophotometry confirmed identity of GO on Al_GO/P substrates

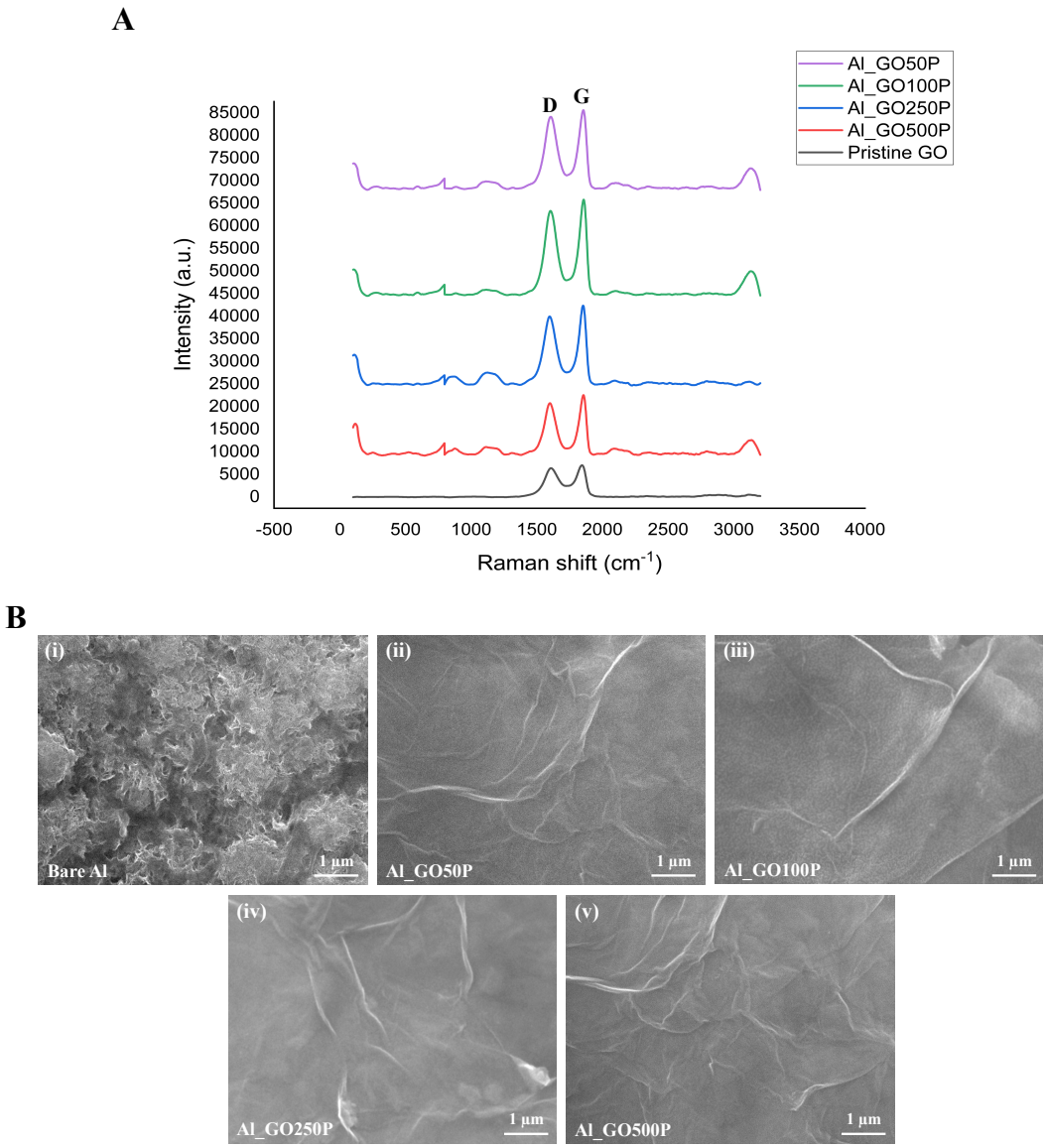

Figure 2. (A) Raman spectra of graphene oxide (GO) and Al_GO/P substrates. The figure shows the Raman signatures (D and G peaks) of GO and the fabricated Al_GO/P substrates at different Y-offset positions. **(B) FESEM micrographs of bare Al vs Al_GO/P surfaces.** FESEM images showcase (i) polished Al, and uniform deposition of GO on Al_GO/P substrates: (ii) Al_GO50P, (iii) Al_GO100P, (iv) Al_GO250P, and (v) Al_GO500P.

Raman spectroscopy serves as a widely employed tool for acquiring structural insights into carbon-based materials. The Raman spectra of graphitic carbon-based materials primarily

manifest the G and D peaks, and their overtones. In Figure 2A, we present the Raman spectra of GO and various Al_GO/P substrates. Notably, the most prominent peaks emerge as the G band, occurring at approximately 1594 cm^{-1}, and the D band, situated around 1328 cm^{-1} as evidenced in prior literature[44,51]. The G peak primarily arises from the bond stretching of sp^2 carbon atom pairs, encompassing both ring and chain structures[75]. In contrast, the D peak is indicative of structural defects within the graphene lattice. Moreover, the variation in intensity ratios of the D and G bands reveal the characteristics of GO deposited on Al_GO/P substrates as shown in Table S1 (Supporting Information). GO exhibited an I_D/I_G ratio of 0.91, which increased slightly to 0.92 for Al_GO50P, then decreased to 0.88 for Al_GO100P, and further to 0.86 for both Al_GO250P and Al_GO500P (Table S1, Supporting Information). These results confirm the successful deposition of GO on the various Al_GO/P surfaces as shown in prior literature[44,76].

Additionally, we verified the identity of commercial PEDOT:PSS via Raman spectroscopy (Figure S1, Supporting Information). The most prominent Raman band, located around 1437 cm^{-1}, consistently exhibits a well-reproducible symmetric profile with a mixed pseudo-Voigt line shape (Figure S1, Supporting Information). Interestingly, this prominent band also displays the most substantial variation, encompassing a total shift of approximately 10 cm^{-1} within the PEDOT:PSS complex. Furthermore, our observations of the Raman signatures for the PEDOT:PSS utilized in this study are in strong concurrence with the Raman spectrum obtained from previous research[77,78]. This agreement underscores the reliability and consistency of the Raman spectroscopic characteristics of the PEDOT:PSS material used in the coating process.

3.1.3. FESEM confirmed uniform deposition of GO on Al surfaces

Electrochemical deposition (ECD) of GO on Al surface is expected to produce a smooth and uniform coating, as the quality of the coating is determined by its homogeneity[48,79]. FESEM

micrographs of the bare Al and Al_GO/P substrates are shown in Figure 2B, providing visual evidence of GO nano-sheets overlaying on the Al substrate The polished Al surface exhibits a non-uniform and rough surface morphology characterized by the presence of potholes and cavities.. However, the FESEM images of Al_GO/P substrates demonstrated smooth GO sheets with small wrinkles and folded at the edges as is evidenced from existing literature[44,50]. FESEM micrographs, therefore, confirmed the uniformity of the GO coatings on Al_GO/P surface.

3.1.4. Hydrophobic and Conductive nature of Al_GO/P surfaces confirmed by water contact angle (WCA) and four-probe conductivity measurements

The deposition of GO on Al substrates has been observed to enhance the surface hydrophobicity[44]. This increase in hydrophobicity is attributed to the uniform GO coating, which alters the surface energy and reduces wettability[80,81]. Consequently, we evaluated the wettability of the bare Al surface and the Al_GO/P substrates, relying on the stationary WCA measurements (Table 2 and Figure S2, Supporting Information). The water contact angle of bare Al was 85.1° but increased to over 90° for all Al_GO/P surfaces, showing an increase in surface hydrophobicity (Table 2 and Figure S2, Supporting Information). Among the samples, Al_GO500P had the highest WCA at 120.2°, followed by Al_GO250P (114.9°), Al_GO100P (106.8°), and Al_GO50P (101.6°).

Additionally, the electrical conductivity measurements for bare Al and Al_GO/P substrates are detailed in Table 2. It is worth noting that pure aluminum possesses inherently high electrical conductivity, registering at 3.43×10^{7} S/m (equivalent to 59.14% of the International Annealed Copper Standard, IACS), consistent with previous literature[82]. The conductivity of the aluminum alloy AA1050 was determined to be 3.11×10^{7} S/m, which is slightly lower than that of pure aluminum but falls within the same order of magnitude. It was observed that while the

conductivity of the Al_GO/P substrates shows a relative reduction compared to the bare Al surface used in this study, the values were within the conductivity ranges for known materials [83–85]. Moreover, this reduction in conductivity becomes more obvious with increasing GO concentration as detailed in Table 2. This phenomenon can be attributed to the inherent insulating nature of graphene oxide, as previously documented[86]. It is plausible that the reduction in conductivity is a consequence of the expansion of interlayer spacing among the GO nanosheets due to the presence of functional groups within the basal planes[87].

Table 2. Stationary water contact angle (WCA) and electrical conductivity values of the synthesized Al_GO/P substrates and control surface, bare Al.

Samples	***WCA (in degrees)***	***Electrical Conductivity* (S/m) x 10^7**
Bare Al	*85.1 ± 0.42*	*3.11 ± 0.67*
Al_GO50P	*101.6 ± 0.95*	*2.17 ± 0.47*
Al_GO100P	*106.8 ± 0.21*	*1.95 ± 0.19*
Al_GO250P	*114.9 ± 4.53*	*1.78± 0.2*
Al_GO500P	*120.2 ± 2.88*	*1.61 ± 0.43*

3.1.5. Porosity evaluation of Al_GO/P substrates

The presence of porosity in coatings directly correlates to lower density and reduced compactness of the coating than the bulk metal[55]. Moreover, a porous coating decreases their protective ability as it allows foreign particles, microorganisms, or corrosive ions to reach and potentially damage the underlying metal, and cause corrosion. The corrosion potential (E_{corr}) and anodic potential (β_a) for pure aluminium and Al_GO/P substrates were determined through Tafel fitting of the linear polarization responses in Figure S3 (Supporting Information) using

EC-Lab software. Polarization resistances were derived from the Nyquist impedance plot (Figure S4, Supporting Information) via Z-Fitting in EC-Lab software.

The details for the porosity measurements for GO coatings is described in the Experimental Section and the results are provided in Table 3. The Al_GO/P substrates exhibited porosities of 60.2% (Al_GO50P), 34.7% (Al_GO100P), 10.9% (Al_GO250P), and 9.5% (Al_GO500P), demonstrating a significant reduction in porosity with increased GO concentration(s) on the Al surface(s). As per prior literature porosity measurements have been correlated to the antimicrobial efficacy of coated materials[44,88].

Table 3. Electrochemical characteristics of bare Al and Al_GO/P substrates and porosity (%) calculation

Sample	Polarization Resistance, R_{PS}	Polarization Resistance, R_P	Corrosion Potential, $E_{corr,Al}$ (V)	Corrosion Potential, $E_{corr,Coatings}$ (V)	Anodic Potential, $\beta_{a,Al}$ (mV)	Porosity (%)
Al_GO50P	1670	2765	-0.73	-0.47	158.3	60.2
Al_GO100P	1670	4788	-0.73	-0.47	158.3	34.7
Al_GO250P	1670	15330	-0.73	-0.48	158.3	10.9
Al_GO500P	1670	17550	-0.73	-0.48	158.3	9.5

3.2. Assessment of antimicrobial potential of Al_GO/P substrates

3.2.1. Al_GO/P inhibited growth of microbial cells

In a preliminary study, growth inhibition assay was conducted to evaluate the antimicrobial activity of the fabricated Al_GO/P substrates. This is a conventional technique where microbial cells are exposed to substrates for a specific time, followed by growth on nutrient rich medium overnight[50]. The antibacterial and antifungal activities of Al_GO/P substrates (Al_GO50P, Al_GO100P, Al_GO250P, and Al_GO500P) were tested against Gram-positive *S. aureus*, Gram-negative *E. coli*, and fungus *C. albicans*. Bare Al (uncoated Al sheet) and glass slides were used as control surfaces.

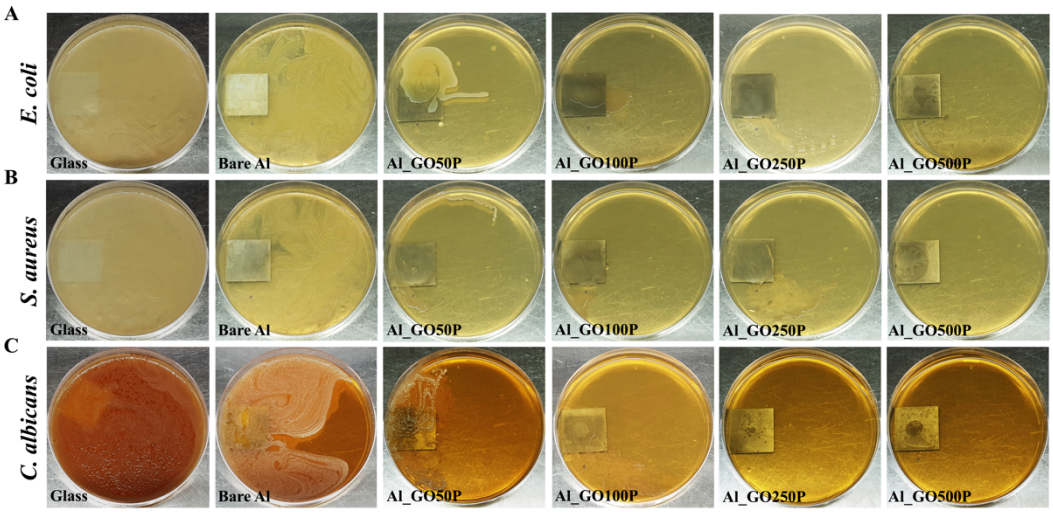

Figure 3. Growth Inhibition Assay of Al_GO/P substrates. After 10 hour of incubation on different control (glass and bare Al) and Al_GO/P substrates, (**A, B**) bacterial (*E. coli, S. aureus*) and (**C**) fungal (*C. albicans*) cells were cultured on LB and YPD agar plates, respectively. The inhibitory roles of the coated substrates were assessed by examining colony growth the following day. Cells cultivated on glass and bare Al surfaces exhibited abundant bacterial and fungal colonies, indicating a lack of antimicrobial potential. In contrast, cells cultured on Al_GO50P presented minimal colony growth while rest of the Al_GO/P substrates demonstrated no visible colony growth.

Figure 3A, 3B and 3C show the bacterial (Gram-positive *S. aureus* and Gram-negative *E. coli*) and fungal (*C. albicans*) colonies on LB and YPD agar plates, respectively. Control surfaces glass and bare Al displayed rich growth of microbial colonies for both bacterial and fungal species. However, significantly low colony growth was observed on Al_GO50P substrate. Further, no bacterial and fungal cell growth were noted on rest of the Al_GO/P substrates. Thus, the growth inhibitory activity of these substrates was conserved across all the microbial species with Al_GO100P, Al_GO250P, and Al_GO500P exhibiting a higher inhibitory potential compared to controls (glass and bare Al), whereas Al_GO50P displayed a moderate inhibitory effect.

607 For a comparative analysis, microbial growth inhibition was performed in presence of pristine
608 GO as shown in Supporting Information (Figure S5A). Relative to the activity of GO, the
609 fabricated substrates were shown to exhibit superior antimicrobial potential towards both
610 bacterial and fungal cells. Besides, evaluation of PEDOT:PSS activity revealed no intrinsic
611 antimicrobial potential over a wide concentration range (1 µg/mL, 50 µg/mL, 100 µg/mL, 250
612 µg/mL, 500 µg/mL, 1 mg/mL, and 2 mg/mL) (Figure S5B, Supporting Information). Therefore,
613 the relative efficacy of Al_GO/P substrates could be correlated to varied concentrations of GO
614 on Al_GO/P substrates correlating to earlier literatures[89,90].

615

616

617

618

619

620

621

622

623

624

625

626

627

3.2.2. Al_GO/P substrates demonstrate potent antibiofilm activity

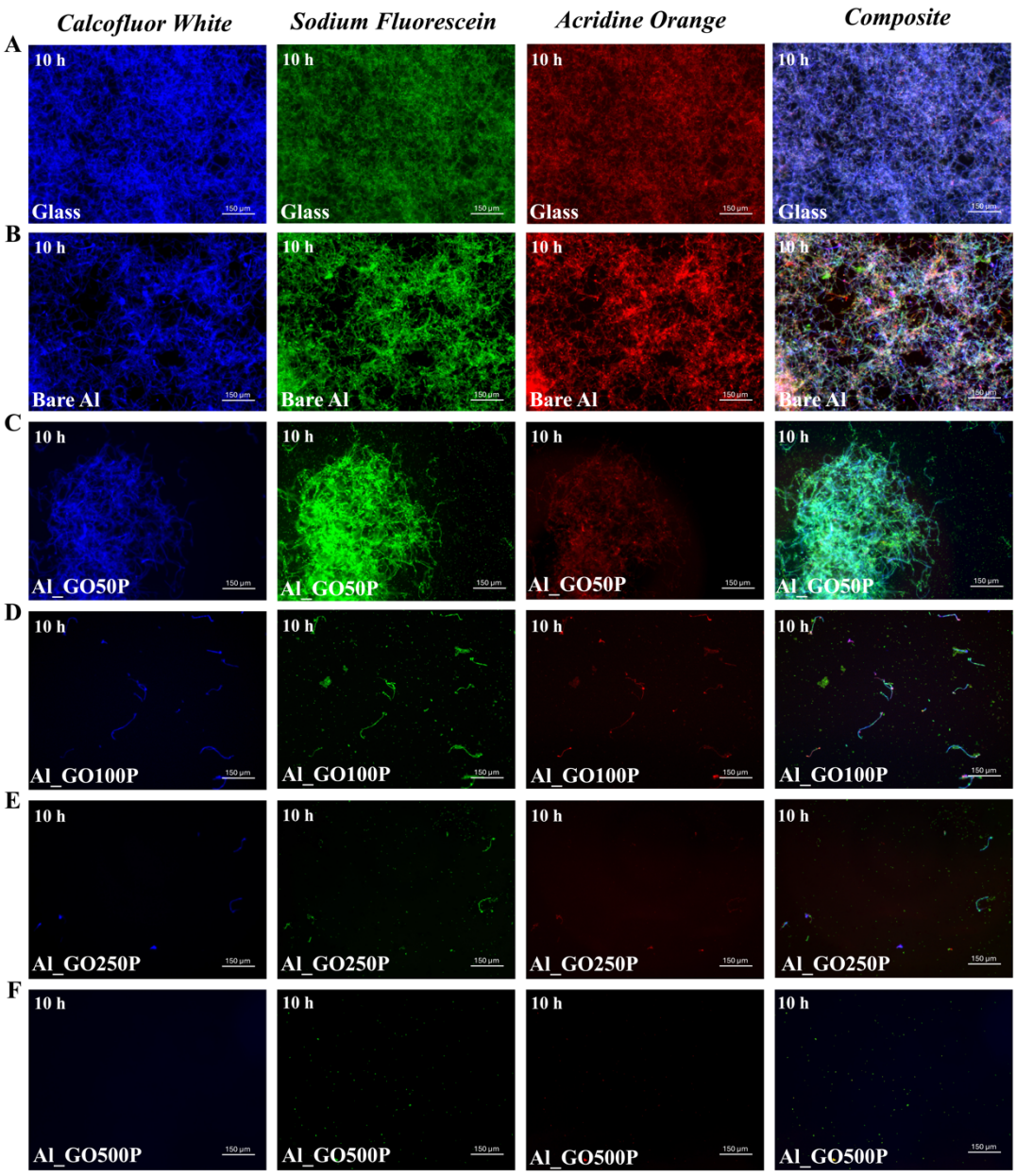

Figure 4. Fluorescence microscopic images of mixed species (*C. albicans*, *S. aureus*, and *E. coli*) biofilm formation (10^7 CFU). Mixed candida-bacterial suspensions were exposed, (**A, B**) to control surfaces (glass and bare Al), and (**C–F**) to various Al_GO/P substrates. Post-exposure, mixed species biofilm were allowed to grow for 10 hours under biofilm stimulating conditions after which the samples were stained with calcofluor white (*blue*), acridine orange (*red*), and sodium fluorescein (*green*) to visualize *C. albicans*, *S. aureus*, and *E. coli*, respectively. Biofilms were imaged using an in-house fluorescence microscope at 40× magnification.

Biofilms are mixed community of microbial population adherent to various biotic and abiotic surfaces[2]. These organized microbial structures play a crucial role in infection dissemination, antibiotic resistance, and may pose a threat to the host's immune system[91]. As previously reported, the antimicrobial efficacy of GO has been well documented across literature[92–95]. In this study, we have evaluated the activity of GO-PEDOT:PSS coated Al (Al_GO/P) surfaces towards mixed species (*Candida*-bacterial) biofilm formation. The antimicrobial activity of the synthesized Al_GO/P surfaces was evaluated against *C. albicans*, *S. aureus*, and *E. coli* by examining the progress of biofilm maturation over a period of 10 hours under biofilm stimulating conditions.

Fluorescent stains were used to visualize Gram-positive *S. aureus* (acridine orange, red), Gram-negative *E. coli* (sodium fluorescein, green), and fungus *C. albicans* (calcofluor white, blue). Control surfaces, such as glass (Figure 4A) and bare Al (Figure 4B), demonstrated dense biofilm formation consisting of bacterial cells within intricate fungal hyphae. This indicates robust microbial colonization on these surfaces that provide a favorable environment for biofilm maturation. On the contrary, significant biofilm inhibition was observed on Al_GO/P substrates. A complete disruption of biofilm structure with only a few adherent microbial cells were noted in presence of Al_GO500P (Figure 4F), closely followed by Al_GO250P (Figure 4E), Al_GO100P (Figure 4D). A moderately inhibited biofilm structure was visualized in presence of Al_GO50P (Figure 4C).

Further to show the robust activity of Al_GO/P, antibiofilm potential was examined at a higher microbial load of 10^8 CFU (Figure S7, Supporting Information). The extent of antibiofilm activity of Al_GO/P substrates were comparable when tested with 10^7 CFU and 10^8 CFU of mixed microbial population. These findings further support the broad-spectrum antimicrobial nature of the Al_GO/P substrates as shown by growth inhibition assay, while substrates with higher GO concentrations yield a more pronounced biofilm inhibitory effect.

Next, crystal violet (CV) staining technique was performed to quantitate mixed species (10^7 CFU) biofilm formation over various test substrates. Glass was used as a positive growth control exhibiting 100% biofilm formation. It was observed that biofilm biomass was lowest when exposed to Al_GO500P, decreasing significantly to 14.3% ($p < 0.0001$), indicating the highest inhibitory activity among the tested Al_GO/P surfaces (Figure S6 and Table S2, Supporting Information). This was followed by Al_GO250P and Al_GO100P, with biomass reductions to 39.3% and 48.5%, respectively ($p < 0.0001$ for both). The biofilm biomass was reduced to 91.3% ($p > 0.05$) in presence of Al_GO50P, indicating the least inhibitory effect (Figure S6 and Table S2, Supporting Information). A similar result was obtained at higher microbial inoculum load at 10^8 CFU (Figure S8 and Table S2, Supporting Information).

Current results highlights a clear correlation between increasing GO concentration on Al surface and its inhibitory effect on biofilm formation. Al_GO50P appears to have a non-significant ($p > 0.05$) role in biofilm inhibition, whereas Al_GO/P substrates with higher concentration of GO (100, 250, and 500 μg/mL) could remarkably inhibit biofilm formation. Besides, a non-significant ($p > 0.05$) inhibition of biofilm formation over bare Al (Figure S6, Figure S8 and Table S2, Supporting information) suggested a superior antibiofilm activity of Al_GO/P surfaces. Additionally in a comparative study, we used GO solutions at corresponding concentrations, which resulted in non-significant ($p > 0.05$) inhibition of biofilm formation relative to control surface glass (Figure S9 and Table S2, Supporting Information). A pairwise analysis of antibiofilm efficacy between pristine GO and test surfaces indicated significant inhibition ($p < 0.0001$) induced by Al_GO/P at corresponding concentration (Figure S10, Supporting Information). The quantitative data for these results at two different inoculum concentrations along with the biofilm inhibitory potential of pristine GO are provided in Table S2, Supporting Information.

Summarizing the results from the growth inhibition (Figure 3) and antibiofilm assays, Al_GO100P, Al_GO250P, and Al_GO500P substrates exhibit superior antimicrobial activity compared to Al_GO50P and control surfaces. This is possibly due to the suppression of microbial colonization and biofilm maturation in the presence of Al_GO/P substrates[44]. Moreover, the lower porosity (Table 3) of Al_GO/P (especially Al_GO100P, Al_GO250P, and Al_GO500P) may have contributed to this enhanced effect, by limiting microbial attachment and biofilm formation. Further analysis via SEM is required to visualize the membrane-damaging (biocidal) activity of Al_GO/P, as demonstrated in the following section.

3.2.3. Al_GO/P substrates induced cell membrane damage in mixed species microbial cell population

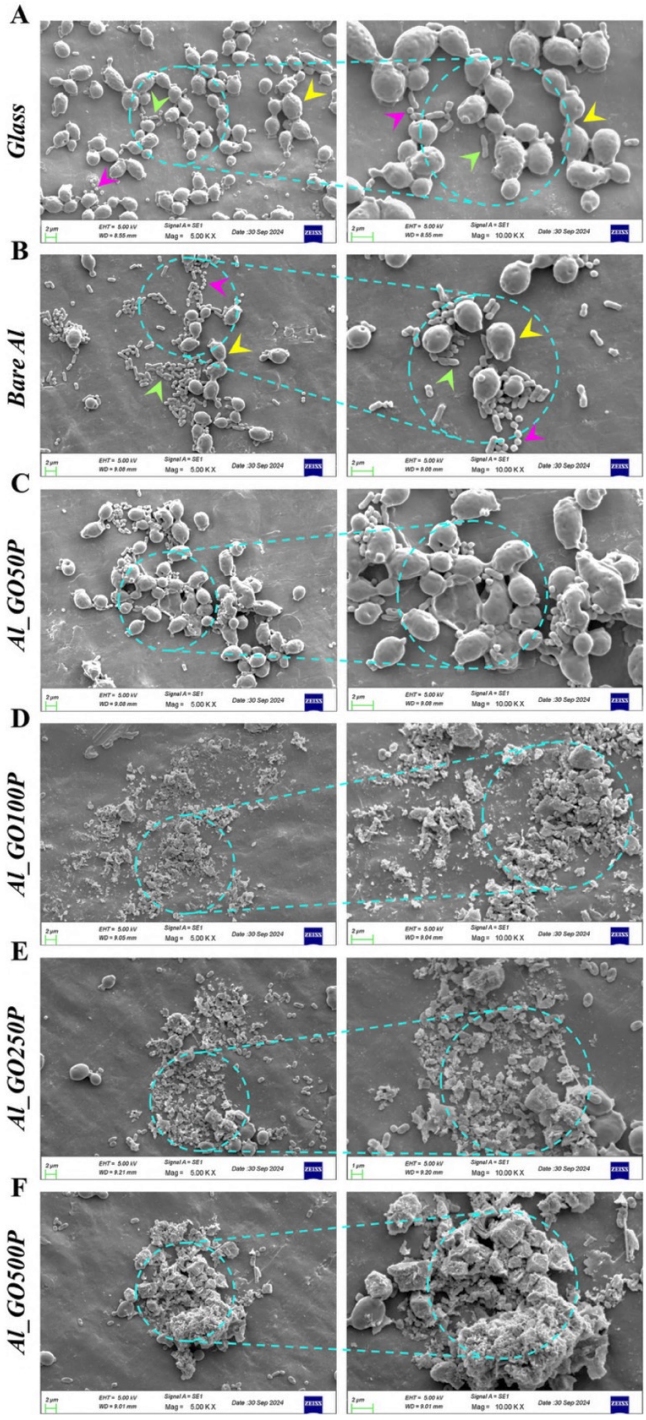

Figure 5. SEM analysis to visualize mixed microbial (*C. albicans*, *S. aureus*, and *E. coli*) cells. Representative SEM micrographs show the morphology of mixed *C. albicans* (*arrowheads, yellow*), *S. aureus* (*arrowheads, pink*), and *E. coli* (*arrowheads, green*) cells after 10 hours of exposure to different control and test substrates: (**A**) Glass, (**B**) Bare Al, (**C**) Al_GO50P, (**D**) Al_GO100P, (**E**) Al_GO250P, and (**F**) Al_GO500P. Images captured at 5000×

and 10,000× magnifications (*dashed circles, cyan*) revealed extensive membrane damage, and complete loss of cellular architecture in microbial cells exposed to Al_GO100P, Al_GO250P and Al_GO500P, compared to the intact morphology observed on control surfaces (Glass, Bare Al). Exposure to Al_GO50P resulted in minor morphological alterations, such as fused and wrinkled cell structures.

In a comprehensive study examining the effects of Al_GO/P surfaces on bacterial and fungal cells, SEM was employed to analyze alterations in cellular architecture and membrane integrity. SEM analysis revealed that cells exposed to the control surfaces (glass, bare Al) maintained their normal cellular morphology, appearing healthy and uniform (Figure 5A and 5B). Exposure to Al_GO50P, displayed less severe but notable morphological damage, including fused cells with wrinkled appearance (Figure 5C). In contrast, exposure to the Al_GO100P (Figure 5D), Al_GO250P (Figure 5E), and Al_GO500P (Figure 5F) induced significant damage to cell membrane with complete loss of cellular architecture for all (*C. albicans*, *S. aureus*, and *E. coli*) cell types. The study demonstrated consistent biocidal activity of the test substrates (Al_GO100P, Al_GO250P, Al_GO500P) towards a mixed microbial population consisting of Gram-positive and Gram-negative bacteria, as well as fungi.

The enhanced antimicrobial potential including biocidal activity of Al_GO/P can be correlated to superior surface hydrophobicity at higher GO concentrations (Table 2 and Figure S2, Supporting Information). This may have facilitated sustained interactions between the microbial cell wall and the Al_GO/P surface, thereby compromising membrane integrity[96]. Besides, we cannot exclude the possibility of electron transfer events occurring in a conductive background of the Al_GO/P substrates, which may lead to the generation of reactive oxygen species (ROS), as shown in previous literature[44,50]. Next, we investigated ROS generation at the substrate interface and intracellularly to further validate the underlying inhibitory mechanism of the Al_GO/P substrates.

3.2.4. Al_GO/P substrates induce intracellular and surface ROS production

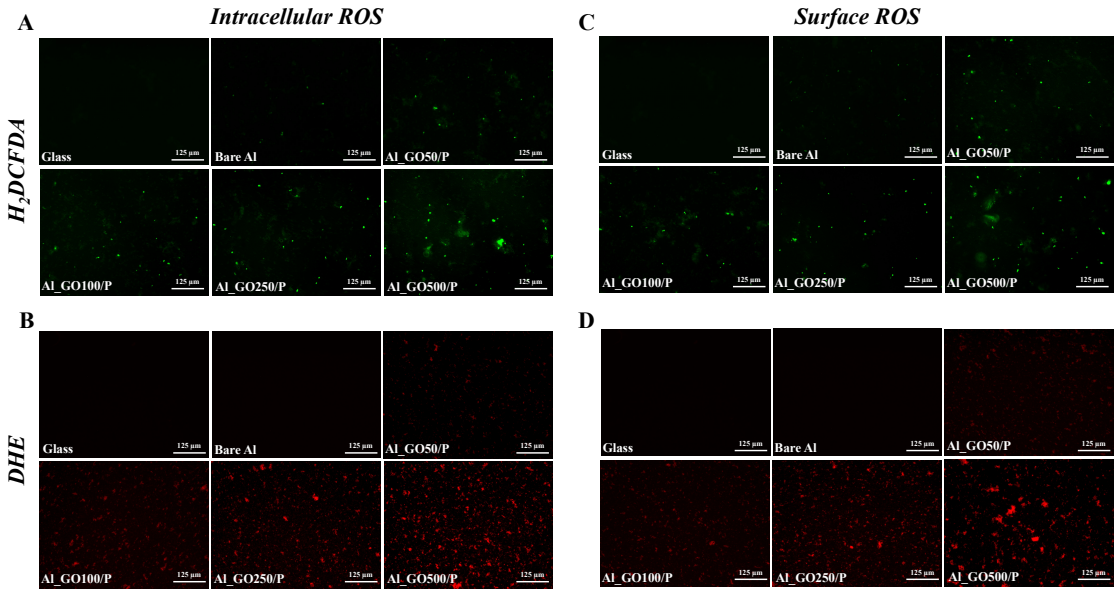

Figure 6. Evaluation of (A, B) intracellular, and (C, D) surface ROS production on Al_GO/P substrates using H_2DCFDA and DHE dye. Following exposure to various test and control surfaces **(A)** Mixed microbial cell population (*C. albicans*, *S. aureus*, and *E. coli*) were stained with H_2DCFDA dye (green cells), and **(B)** mixed bacterial cells consisting of *S. aureus* and *E. coli* were stained with DHE dye (red cells), for detection of intracellular ROS production. No ROS production was observed on glass, and only minimal signal was detected on Al relative to the test substrates. Abundant fluorescent signals correlating to intracellular ROS generation were observed for the bacterial and fungal cells exposed to Al_GO500P, Al_GO250P, and Al_GO100P surfaces using H_2DCFDA (green) and DHE (red) fluorescent dyes. Al_GO50P induced relatively lesser number of fluorescent cells; Detection of ROS production on the surface of Al_GO/P substrates after a 10-hour of exposure to **(C)** mixed population of cells (*C. albicans*, *S. aureus*, and *E. coli*) using H_2DCFDA dye (green fluorescence), and **(D)** mixed bacterial cells (*S. aureus* and *E. coli*) with DHE dye (red fluorescence). ROS indicator dyes H_2DCFDA and DHE were applied on different test and control surfaces. No ROS production was noticed on the surface of Glass and Al relative to test substrates. Varied levels of abundant fluorescent signals correlating to ROS generation were observed on the surface of Al_GO500P, Al_GO250P, and Al_GO100P as revealed by H_2DCFDA (green) and DHE (red) stains. Relatively mild signal was detected on the surface of Al_GO50P. Cells were imaged using in-house fluorescence microscope at 40× magnification.

The catalytic generation of ROS at metal-environment interfaces is a well-characterized process, mediated by physicochemical interactions that promote oxidative stress conditions[97,98]. These interactions involve complex mechanisms, including redox reactions

822 and surface modifications, which could mediate the transfer of electrons and lead to the
823 formation of ROS[50]. The production of ROS can have significant implications for both the
824 metal surfaces and the biological systems they interact with, potentially affecting cellular
825 responses[97]. In this work, ROS production was evaluated using the indicator dye 2',7'-
826 dichlorodihydrofluorescein diacetate (H_2DCF-DA) after exposing mixed (bacterial and fungal)
827 microbial cells to various Al_GO/P substrates. This dye is effective in detecting a wide range
828 of ROS, including hydrogen peroxide (H_2O_2), hydroxyl radicals (•OH), and other reactive
829 species such as carbonate radicals and nitric oxide[99]. When ROS are present, the initially non-
830 fluorescent H_2DCF-DA is transformed into the highly fluorescent compound 2',7'-
831 dichlorofluorescein (DCF+), which emits a green signal observable through fluorescence
832 microscopy.

833 In addition, dihydroethidium (DHE) is also utilized for ROS detection. DHE displays blue
834 fluorescence in the cell cytoplasm; however, upon reacting with superoxide anions, it is
835 oxidized to form 2-hydroxyethidium, which intercalates into DNA and exhibits red
836 fluorescence (DHE+). This makes DHE particularly useful for detecting cytosolic superoxide
837 (O_2•$^-$)[99]. It can also undergo nonspecific oxidation by other radicals like peroxynitrite
838 (ONOO−) and hydroxyl radicals (•OH). In this work, H_2DCFDA dye was employed to assess
839 the overall oxidative stress levels in mixed *Candida*-bacterial cell suspensions. Additionally,
840 DHE was utilized specifically to detect cytosolic superoxide in the mixed bacterial cell
841 suspensions (*S. aureus* and *E. coli*).

842 We observed that Al_GO/P substrates, especially Al_GO500P, Al_GO250P, Al_GO100P
843 exhibited a significantly higher number of DCF+ signals indicative of elevated ROS relative
844 to control surfaces both intracellularly (Figure 6A) and at the substrate surface (Figure 6C) in
845 mixed pathogen populations consisting of *S. aureus*, *E. coli*, and *C. albicans*. This was closely
846 followed by Al_GO50P displaying relatively lower number of DCF+ fluorescent cells. The

control Al surface showed minimal DCF+ signal, while the glass surface displayed no detectable DCF+ (green) signal at all. The elevated ROS levels may directly correlate to an electron transfer event from the microbial cells to the GO functional groups over conductive substrates causing surface ROS production. Elevated intracellular ROS production is indicative of cell death and the activation of related cell signaling pathways[100].

We further examined the presence of cytosolic superoxide in a mixed bacterial population both intracellularly (Figure 6B) and at the substrate interface (Figure 6D). Similar to our observation in Figure 6A and 6C, control surfaces such as glass and bare aluminium, did not exhibit any DHE+ (red) cells, indicating a lack of ROS production overall. Conversely, varying numbers of fluorescent DHE+ cells were observed on different Al_GO/P substrates. Notably, Al_GO500P, Al_GO250P, and Al_GO100P induced a higher population of DHE+ cells than Al_GO50P. It is plausible that extending the exposure time on the substrate surface may lead to a greater number of ROS-positive cells.

Previous studies have highlighted the role of ROS in the broad-spectrum antimicrobial activity of graphene and its derivatives[44,101]. In fact, oxidative stress can lead to oxidation of proteins, lipids, and nucleic acids in microbial cells, resulting in irreversible membrane damage and cell death[102]. The pronounced microbiocidal activity observed for Al_GO100P, Al_GO250P, and Al_GO500P substrates can be attributed to the conductivity of these substrates (Table 2), which facilitates electron transfer from the microbial cells to the GO surface, and enhanced ROS production. Besides higher surface hydrophobicity values for these substrates (Table 2), may have promoted a stable microbial interaction causing contact mediated membrane damage and ROS induced stress. Although Al_GO50P exhibited higher conductivity, its antimicrobial performance was less, likely due to its lower surface hydrophobicity, causing an attenuated microbial cell interaction with its surface.

871 **3.3. Assessment of anticorrosion potential of Al_GO/P substrates**

872 *3.3.1. Al_GO/P substrates exhibit biocorrosion resistance*

873 The corrosion rate of the fabricated Al_GO/P substrates was primarily assessed in two
874 designated immersion systems, as detailed in the experimental section. Our objective was to
875 analyse the corrosion kinetics of these materials in an abiotic system, which consisted solely
876 of growth media and antibiotics to inhibit any microbial growth. This setup allowed us to
877 evaluate the chemical corrosion properties of Al_GO/P surfaces in a controlled environment,
878 free from biological contamination. Parallelly, we investigated a biotic system that included
879 microbial cells to assess microbiologically influenced corrosion (MIC) potential of Al_GO/P
880 substrates. This dual approach not only provides a comprehensive understanding of the
881 corrosion behaviour of the fabricated Al_GO/P substrates but also highlights their potential
882 effectiveness in real-world applications, where both chemical (abiotic) and biological (biotic)
883 factors influence corrosion rates[103]. In addition to evaluating the synthesized Al_GO/P
884 substrates, we included two control materials in this study: bare aluminium, and cold-rolled
885 steel (CR Steel), which is recognized as a highly corrosive material and serves as a control in
886 corrosion studies due to its known susceptibility to corrosion[104]. Although both chemical
887 corrosion and MIC involve material degradation, chemical corrosion generally proceeds faster
888 and more aggressively due to its direct chemical interactions with the metal surface, especially
889 in high-temperature or harsh environments[105]. Whereas MIC, also an electrochemical process,
890 relies on the activity of microorganisms and their metabolites to promote corrosion, often under
891 specific conditions[25].

892

893

894

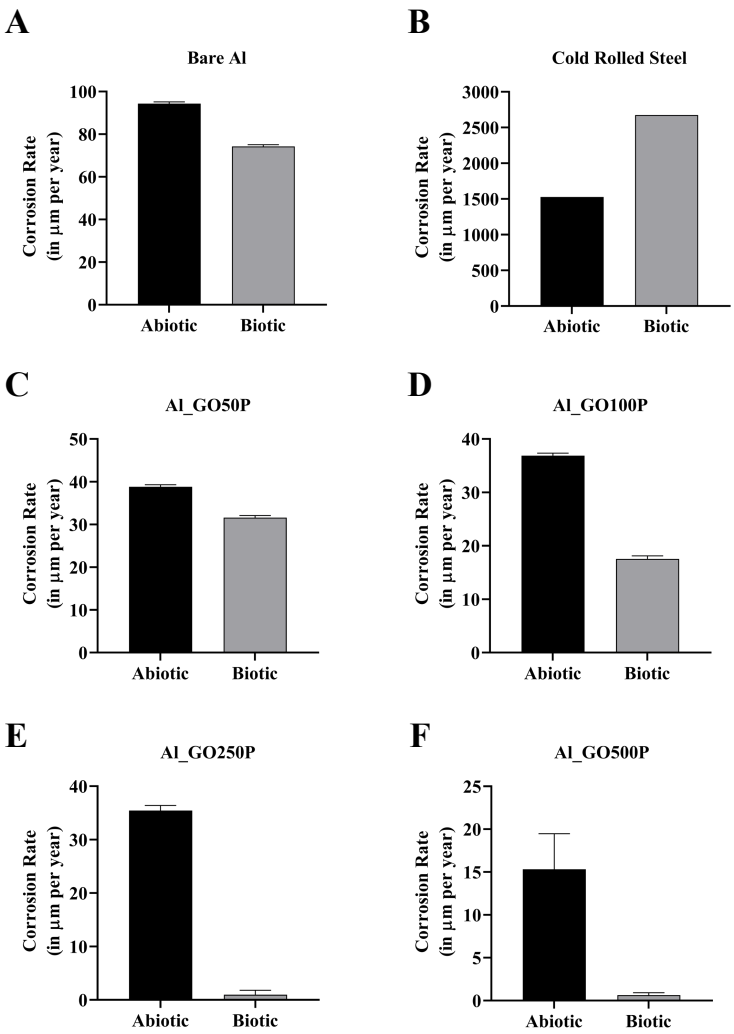

Figure 7. Corrosion rates of various control and Al_GO/P substrates in µm per year after 45 days of exposure to abiotic and biotic environments. Error bars represent ±1 standard deviation (SD) from mean for three independent biological replicates (n=3).

Figure 7 illustrates the corrosion rates of various substrates after 45 days of immersion in the studied systems, highlighting the effects of both abiotic and biotic conditions. In the abiotic system, the corrosion rates were measured as follows: 94.3 ± 0.8 µm/year for aluminium (Figure 7A), 1528.3 ± 0.1 µm/year for CR Steel (Figure 7B), 38.8 ± 0.5 µm/year for Al_GO50P (Figure 7C), 36.9 ± 0.5 µm/year for Al_GO100P (Figure 7D), 35.4 ± 1.0 µm/year for

Al_GO250P (Figure 7E), and 15.3 ± 4.1 μm/year for Al_GO500P (Figure 7F). In contrast, the corrosion rates in the biotic system were recorded as follows: 74.2 ± 0.8 μm/year for aluminium (Figure 7A), 2674.2 ± 0.3 μm/year for CR steel (Figure 7B), 31.6 ± 0.5 μm/year for Al_GO50P (Figure 7C), 17.6 ± 0.6 μm/year for Al_GO100P (Figure 7D), 1.0 ± 0.8 μm/year for Al_GO250P (Figure 7E), and 0.6 ± 0.3 μm/year for Al_GO500P (Figure 7F). It was noted that, in general, the immersion systems lacking microbial presence tended to display higher corrosion rates. However, this trend did not apply to CR steel, which is a known corrosive material used as a control in this study and inherently exhibits high corrosion rates. This observation aligns with the understanding that chemical corrosion often occurs at a faster and higher rate than MIC, which is primarily driven by electrochemical reactions in aggressive environments, as mentioned by previous literatures[105–107]. Conversely, the immersion system with microbial load showed a lower corrosion rate, reflecting the variability of MIC, which can be influenced by factors such as the type of microorganisms present and their metabolic by products[24,25]. Corrosion rates for the Al_GO/P substrates immersed in the abiotic system corresponded to a moderate corrosion intensity as defined by the NACE Standard RP-07-75[67].

The results presented in Figure 7 provide a positive correlation between resistance to MIC and the concentration of GO coatings on Al_GO/P surfaces. In the biotic system, Al_GO500P exhibited the lowest corrosion rate, followed by Al_GO250P, indicating superior protection against MIC; while, Al_GO100P and Al_GO50P showed relatively higher corrosion rates than the other coated substrates, though significantly lower than the controls (bare Al and CR Steel) under both immersion environments. It can be inferred that increasing GO concentration(s) in coatings enhances biocorrosion resistance in Al_GO/P system, likely attributable to enhanced barrier characteristics and reduced microbial adhesion[108–111]. These findings are further supported by results from the antibiofilm assays (Figure 4, Figure S6 and Table S2, Supporting Information) and SEM analysis (Figure 5), which collectively demonstrate enhanced

antimicrobial efficacy and contact-mediated cell membrane damage at higher GO concentrations.

Next, FESEM analysis revealed distinct morphological alterations in control samples (bare Al and CR Steel) compared to the synthesized Al_GO/P substrates following immersion under abiotic (Figure S11, Supporting Information) and biotic (Figure S12, Supporting Information) conditions. These observations align with the corrosion rate analyses (Figure 7), underscoring the superior anticorrosion performance of the GO-PEDOT:PSS functionalized Al system. In contrast, uncoated bare Al and CR Steel exhibited pronounced localized pitting and deep corrosion features, suggesting their susceptibility towards corrosion. The optical images of the control and test substrates before and after immersion in abiotic and biotic environments are presented in Figure S13 (Supporting Information).

Overall, these results underscore the critical role of GO-PEDOT:PSS coating concentration in improving the corrosion resistance of Al substrates in both abiotic and biotic immersion environments. Given that corrosion products are known to directly contribute to cytotoxic effects on human cells[26], and considering the promising corrosion resistance observed in Al_GO/P surfaces, we evaluated the biocompatibility of the Al_GO/P substrates in the upcoming section.

3.4. Cytotoxicity assessment: Al_GO50P and Al_GO100P demonstrate superior biocompatibility

MTT assay is a widely utilized method for assessing cell viability and proliferation, relying on the metabolic activity of living cells[70,112]. This assay involves the reduction of the yellow tetrazolium salt, MTT (3-(4,5-dimethylthiazol-2-yl)-2,5-diphenyltetrazolium bromide), to an insoluble purple formazan product by mitochondrial enzymes present in metabolically active

cells. The amount of formazan produced is directly proportional to the number of viable cells in the sample, allowing for quantification through absorbance measurements at 570 nm.

For biocompatibility assessment, Al_GO1000P, featuring a GO concentration of 1 mg/mL, was included for comparative analysis. We conducted MTT assay with material extracts as well as direct exposure to the substrates to gain a comprehensive understanding of their effects on HEK293T kidney cell lines[113,114]. Given that the release of nanomaterials from antimicrobial surfaces poses a significant concern, potentially leading to systemic toxicity affecting various organs and functional systems, it was crucial to investigate this further[27]. An extract test was performed on control and Al_GO/P substrates to determine whether any substance was leaching from the surface into the growth medium[71]. The cell viability values used to plot the graphs are tabulated in Table S3A and S3B (Supporting information) for indirect (extract) and direct contact assay, respectively.

The assessment of cell viability after exposure to the Al_GO/P material extracts (Al_GO50P, Al_GO100P, Al_GO250P, Al_GO500P, Al_GO1000P) revealed non-significant ($p > 0.05$) impact on cell growth or viability when compared to the control HEK293T cells in growth media alone (Figure 8A and Table S3A, Supporting Information). No changes in HEK293T cell viability were observed upon indirect contact with the glass surface, as anticipated. In contrast, extracts from bare aluminum resulted in a notable decrease in HEK293T cell viability, dropping to 71.9% ($p \leq 0.0001$) and 72.6% ($p \leq 0.0001$) at 24 and 48 hours, respectively; compared to unexposed control cells, which exhibited a viability of 100% at similar time points. As shown by previous literatures, the systemic toxicity concern arises from the ability of bare aluminum to release ions or particles that can disrupt cellular function, leading to reduced viability and potential long-term health effects[115,116]. Current results suggested that fabricated Al_GO/P substrates possess a stable GO-PEDOT:PSS coating, effectively minimizing the risk of harmful leaching and subsequent systemic toxicity.

Additionally, direct contact assay was conducted to validate uses of Al_GO/P materials for potential *in vivo* biomedical applications. Cell viability data presented in Figure 8B and Table S3B, Supporting Information, indicate that exposure to Al_GO50P (89.5% at 24 h and 95.8% at 48 h; $p > 0.05$) and Al_GO100P (90.9% at 24 h and 96.1% at 48 h; $p > 0.05$) resulted in no significant change in HEK293T cell viability compared to the control. In contrast, Al_GO250P (86.7% at 24 h, $p > 0.05$; 84.3% at 48 h, $p = 0.0116$) and Al_GO500P (82.5% at 24 h, $p = 0.0234$; 84.1% at 48 h, $p = 0.0108$) showed a moderate reduction in cell viability over 24-48 hour. Notably, Al_GO1000P (64.9% at 24 h, $p < 0.0001$; 59.1% at 48 h, $p < 0.0001$) caused a significant decrease in HEK293T cell viability. As expected there was no alteration in the viability of cells (HEK293T) in direct contact with the glass surface. HEK293T cells exposed to bare Al demonstrated the lowest cell viability percentage 77.5% at 24 hours ($p = 0.0038$) and 53% at 48 hours ($p \leq 0.0001$) relative to HEK293T cell control. These results collectively highlight the superior biocompatibility of Al_GO50P and Al_GO100P, underscoring their potential for possible biomedical applications. We also conducted comparative studies on the HEK293T cell viability exposed to pristine GO and PEDOT:PSS at corresponding concentrations. The cell viability percentage(s) decreased with increasing concentration(s) of pristine GO and PEDOT:PSS (Figure S14 and S15, Supporting Information) when exposed to HEK293T cells for a period of 24 and 48 hours. Further, PEDOT:PSS at a concentration used to prepare the hybrid coating in this study (1 μg/mL) led to nonsignificant alteration in the cell viability.

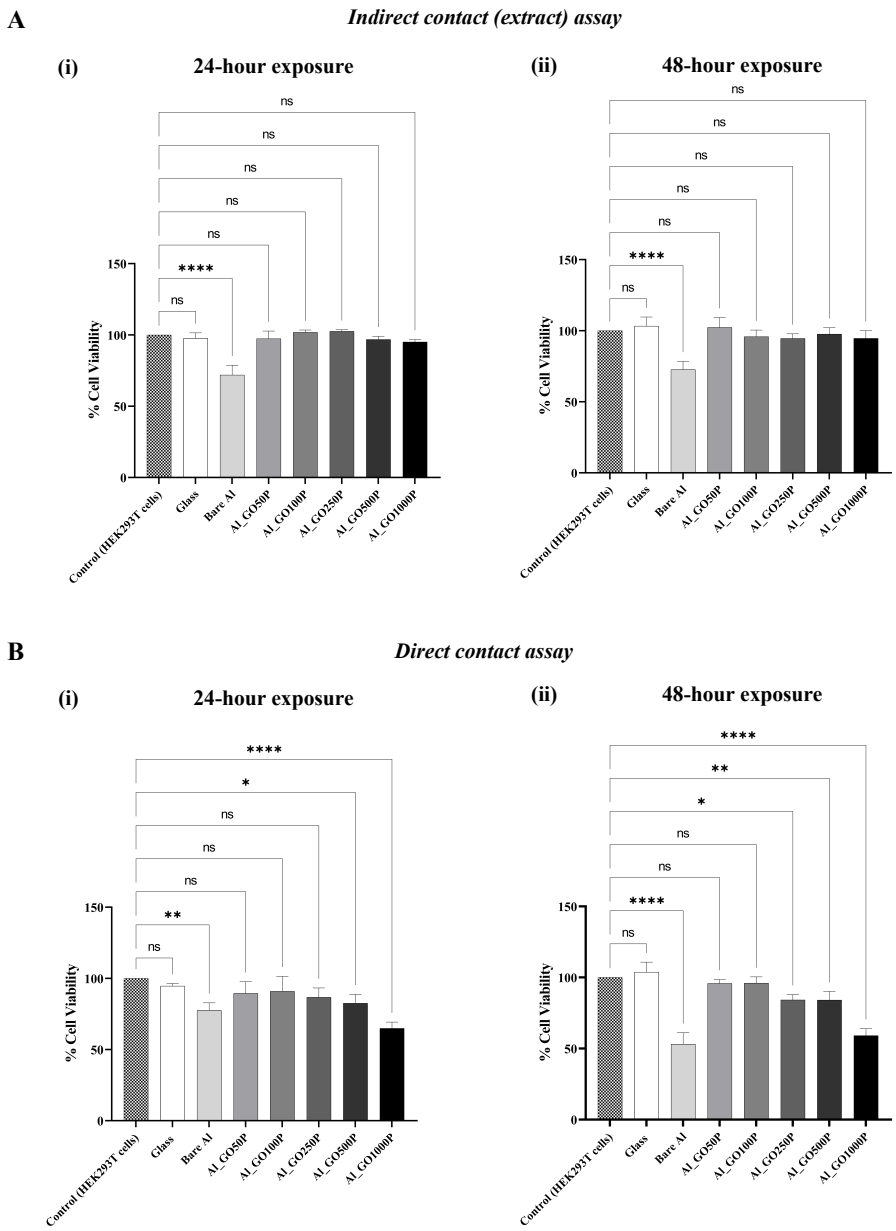

Figure 8. Cytotoxicity evaluation of control and Al_GO/P substrates. Comparison of cell viability, assessed by MTT method in the DMEM culture medium, after exposure to (**A**) Al_GO/P sample extracts by indirect contact assay and (**B**) after direct contact with the Al_GO/P samples; at (**i**) 24-hour and (**ii**) 48-hour. Data are expressed as % values of result obtained in comparison to control cells (HEK293T) not exposed to materials or material extracts. Error bars represent ±1 standard deviation (SD) from mean for three independent biological replicates (n=3). Statistical significance was assessed using one-way ANOVA; specific p-values of <0.05, <0.01, <0.001, and <0.0001 were indicated as *,**,***, and ****, respectively.

1050 Current findings confirm that Al_GO/P surfaces do not exhibit leaching, as evidenced by the
1051 extract (indirect) assay. HEK293T cells exposed to extracts from all Al_GO/P test surfaces
1052 maintained viability comparable to the untreated control group, whereas extracts from bare
1053 aluminium caused a significant reduction in cell viability. The corrosion resistance properties
1054 of the test substrates may have minimized the cytotoxicity effects associated with leaching, as
1055 reported in prior literature[117,118]. Additionally, direct contact assays showed that HEK293T
1056 cells retained normal viability on Al_GO50P and Al_GO100P surfaces, with no statistically
1057 significant differences from the controls. In contrast, direct exposure to bare Al, Al_GO250P,
1058 Al_GO500P, and Al_GO1000P surfaces resulted in marked decrease in cell viability over a
1059 period of 24-48 hour. While Al_GO250P and Al_GO500P exhibited remarkable antibiofilm
1060 properties, their negative effect on cell viability suggests potential cytotoxicity concerns in
1061 direct-contact mediated biomedical applications. Therefore, these surfaces may be more
1062 suitable for *in vitro* or exterior uses where robust antimicrobial activity is essential. Although,
1063 Al_GO50P demonstrated excellent biocompatibility, it lacked significant antimicrobial, and
1064 antibiofilm efficacy (Figure 4), indicating a need for further optimization to enhance its
1065 performance. Overall, Al_GO100P achieved a desirable balance, combining both high
1066 biocompatibility and effective antibiofilm activity, and thus stands out as a promising candidate
1067 for *in vivo* biomedical device applications where cellular compatibility and biofouling
1068 resistance are paramount.

1069 In summary, the results underscore the broader potential of GO-PEDOT:PSS hybrid coatings
1070 on bare Al sheets in healthcare setup. By enhancing biocorrosion resistance and antibiofouling
1071 activity, GO-PEDOT:PSS coatings on Al serve as an effective barrier against microbial
1072 colonization, which is known to accelerate MIC. The capacity of Al_GO/P substrates to
1073 decelerate Al corrosion rates (Figure 7) highlights their potential as versatile materials for
1074 biomedical and orthopedic implants, as well as other medical devices, where sterility and tissue

healing are critical requirements[24,25]. Continued research into the interactions between graphene-based materials and biological systems will be vital for optimizing their use in medical as well as industrial sectors while ensuring safety and efficacy.

4. Conclusion

Biofilms are implicated in 60–70% of nosocomial infections and significantly increase the risk of device-associated complications, leading to higher infection rates, morbidity, and mortality in clinical settings[119]. The resilience of biofilms to conventional antibiotics underscores the urgency for innovative surface technologies that can effectively prevent microbial colonization and reduce HAIs. Considering these challenges, there is a critical need to design and evaluate novel materials possessing broad-spectrum antimicrobial capabilities, minimal to no cytotoxicity, and biocorrosion resistance. This systematic assessment is essential to ensure that the fabricated materials are effective in inhibiting the growth of pathogens while being safe for both *in vitro* and *in vivo* environments.

In the present study, we synthesized and characterized GO-PEDOT:PSS hybrid coating on Al surface using electrochemical deposition method. Analytical techniques like Raman spectrophotometry confirmed the identify of GO nanosheets on Al substrates. FESEM analysis confirmed the uniform morphology of Al_GO/P surfaces. Further, water contact angle and four-probe conductivity measurements highlighted the hydrophobic and conductive nature of the Al_GO/P substrates. Additionally, porosity measurements indicated that Al_GO500P, Al_GO250P, and Al_GO100P had relatively lower porosity Al_GO50P.

Next, we systematically assessed the antibiofouling efficiency of the synthesized Al_GO/P substrates by exposing them to a mixed population of clinically relevant pathogens Gram-positive *S. aureus*, Gram-negative *E. coli* and fungus *C. albicans*. Results from growth

1099 inhibition and antibiofilm assay suggested, superior antimicrobial properties of Al_GO100P,
1100 Al_GO250P, and Al_GO500P compared to Al_GO50P. SEM analysis confirmed the
1101 microbiocidal nature of the test substrates (Al_GO/P) revealing extensive loss of membrane
1102 integrity and impairment of cell morphology in mixed pathogen population, revealing the
1103 microbiocidal nature of the test substrates. As reported earlier, the membrane-damaging
1104 activity of GO involves multiple mechanisms, such as nano-knife or sharp-edge effects,
1105 membrane pore formation, phospholipid extraction, and electron extraction by GO side groups,
1106 which induce oxidative stress[36]. To gather a clear mechanistic understanding and to confirm
1107 the occurrence of electron extraction events, we also conducted intracellular and surface ROS
1108 production assay. The presence of intracellular ROS indicates microbial cell death, whereas the
1109 detection of ROS on the Al_GO/P surface points to an interface phenomenon that confirms
1110 electron transfer directed ROS generation[89].

1111 Summarizing the experimental data, we discuss a possible mechanism underlying the robust
1112 antimicrobial and antibiofilm activity of the fabricated Al_GO/P substrates (Al_GO100P,
1113 Al_GO250P, and Al_GO500P) (Figure 4). Firstly, surface hydrophobicity of the Al_GO/P
1114 substrates promotes stable interactions with microbial cells, which likely facilitates contact-
1115 mediated membrane disruption through sharp-edge effect of GO (Table 2). In addition, the
1116 conductive nature (Table 2) of the synthesized substrates may have induced electron transfer
1117 events that generate ROS (Figure 6), further contributing to microbial cell damage (Figure 5).
1118 Notably, these surfaces were also found to possess fewer porous domains (Table 3), which
1119 limits microbial colonization resulting in a robust antibiofilm activity[88]. Together, these
1120 physical and electrochemical interactions might have synergistically enhanced the
1121 antibiofouling efficacy of fabricated Al_GO/P surfaces. The superior antibiofouling activities
1122 observed for test substrates; Al_GO500P, Al_GO250P, Al_GO100P relative to Al_GO50P can
1123 be linked to higher surface hydrophobicity, and lower porosity (Table 2, Table 3; Figures S2-

S4, Supporting Information). Experimental evaluation of control study using glass, bare Al and pristine GO further ascertain the superior broad-spectrum antibiofouling activity of synthesized Al_GO/P substrates.

To further evaluate the feasibility of real time applications of these substrates, we assessed the biocorrosion resistance under abiotic and biotic environments. Analyses from corrosion rates (Figure 7) and FESEM imaging (Figure S11 and S12, Supporting Information) revealed that the substrates exhibited biocorrosion resistance in the order; Al_GO500P, Al_GO250P, Al_GO100P, and Al_GO50P compared to controls (bare Al and CR Steel). The improved corrosion resistance of Al_GO/P surfaces can be attributed to their reduced porosity (Table 3), which results in decreased microbial contamination and, consequently, a lower MIC (Figure 7; Figures S11, S12, Supporting Information).

Next, it was crucial to conduct biocompatibility testing to ensure the safety and suitability of Al_GO/P within physiological environment. Thus, we assessed the potential cytotoxicity of the synthesized surfaces by performing MTT assay. Al_GO100P was identified as a promising candidate for *in vivo* implant material, owing to its excellent biocompatibility (Figure 8) along with remarkable antibiofilm (Figure 4) and anticorrosion properties (Figure 7 and Figure S11 and S12, Supporting Information). In contrast, the reduced cell viability observed with Al_GO250P and Al_GO500P suggests a potential for cytotoxicity, making them better suited for *ex vivo* applications.

In toto, the findings from this study demonstrate the potential of GO-PEDOT:PSS hybrid coatings for enhancing the biocorrosion resistance, antibiofouling, and biocompatibility of Al surfaces. The GO-PEDOT:PSS/Al hybrid surfaces could effectively improve corrosion resistance by forming an impermeable layer that may have prevented the attachment of microbial species inhibiting MIC. The synthesized hybrid substrates may provide a promising

approach for improving the durability and performance of Al; particularly where corrosion resistance, antibiofilm properties, and biocompatibility are crucial, such as in the medical, water treatment, and industrial sectors. Further research and optimization of the Al_GO/P composite system could facilitate the development of advanced aluminum-based materials specifically tailored for healthcare applications, particularly in the design of next-generation biomedical implants with improved material lifespan.

Author Contributions

S.S.N., Conceptualization; Methodology; Validation; Formal analysis; Investigation; Resources; Data curation; Writing original draft; Writing review and editing; Visualization. **R.E.A.**, Conceptualization; Validation; Formal analysis; Writing original draft; Writing review and editing. **T.N.N.**, Conceptualization; Validation; Formal analysis; Resources; Writing original draft; Writing review and editing. **S.N.**, Conceptualization; Methodology; Validation; Formal analysis; Investigation; Resources; Writing original draft; Writing review and editing; Supervision; Project administration; Funding acquisition.

Acknowledgements

Aluminum substrates were provided by NALCO India, Ltd. The authors gratefully acknowledge the School of Basic Sciences at IIT Bhubaneswar for granting access to their facilities for substrate synthesis and porosity evaluation. Sincere thanks are extended to the central facilities at TIFR Hyderabad for their valuable support in the characterization of Al_GO/P substrates. The authors also appreciate the Central Research Facility at KIIT-DU, Bhubaneswar, for providing access to the scanning electron microscope (SEM). The infrastructure grant from the Department of Biotechnology, Government of India, under the Boost to University Interdisciplinary Life Science Departments for Education and Research (BUILDER) program at KIIT School of Biotechnology is also duly acknowledged. S.S.N. was supported by DD Innovation Incorporated, U.S.A. (Ref No: DD/KIIT/001/2023).

Conflict of Interest Statement

The authors declare that they have no conflict of interest.

Data Availability Statement

All data sources are cited within this article and its Supporting Information.

References

[1] *N. C. Bamford, C. E. Macphee, N. R. Stanley-Wall, Microbiology (United Kingdom)* ***2023****, 169, 001338, DOI: 10.1099/MIC.0.001338/CITE/REFWORKS.*

[2] *L. Karygianni, Z. Ren, H. Koo, T. Thurnheer, Trends Microbiol* ***2020****, 28, 668, DOI: 10.1016/J.TIM.2020.03.016.*

[3] *HAIs: Reports and Data | HAIs | CDC, https://www.cdc.gov/healthcare-associated-infections/php/data/index.html, accessed May 5,* ***2025****.*

[4] *L. Guarente, C. Mosconi, M. Cicala, C. De Santo, F. Ciccacci, M. Carestia, L. Emberti Gialloreti, L. Palombi, G. Quintavalle, D. Di Giovanni, E. Buonomo, S. Moramarco, F. Riccardi, S. Orlando, Infection Prevention in Practice* ***2024****, 6, 100391, DOI: 10.1016/J.INFPIP.2024.100391.*

[5] *A. Cassini, D. Plachouras, T. Eckmanns, M. Abu Sin, H. P. Blank, T. Ducomble, S. Haller, T. Harder, A. Klingeberg, M. Sixtensson, E. Velasco, B. Weiß, P. Kramarz, D. L. Monnet, M. E. Kretzschmar, C. Suetens, PLoS Med* ***2016****, 13, e1002150, DOI: 10.1371/JOURNAL.PMED.1002150.*

[6] *Healthcare-associated infections in European hospitals (PPS survey) 2022-2023, https://www.ecdc.europa.eu/en/publications-data/healthcare-associated-infections-european-hospitals-pps-survey-2022-2023, accessed May 5,* ***2025****.*

[7] *Each year, 4.3 million patients in hospitals in the EU/EEA are affected by healthcare-associated infections, https://www.ecdc.europa.eu/en/news-events/each-year-43-million-patients-hospitals-eueea-are-affected-healthcare-associated, accessed May 5,* ***2025****.*

[8] *R. M. Klevens, J. R. Edwards, C. L. Richards, T. C. Horan, R. P. Gaynes, D. A. Pollock, D. M. Cardo, Public Health Reports* ***2007****, 122, 160, DOI: 10.1177/003335490712200205.*

[9] *Global report on infection prevention and control 2024, https://www.who.int/publications/i/item/9789240103986, accessed May 5,* ***2025****.*

[10] *HAI National Action Plan, https://www.hhs.gov/oidp/topics/health-care-associated-infections/hai-action-plan/index.html, accessed May 5,* ***2025****.*

[11] *P. Mathur, P. Malpiedi, K. Walia, P. Srikantiah, S. Gupta, A. Lohiya, A. Chakrabarti, P. Ray, M. Biswal, N. Taneja, P. Rupali, V. Balaji, C. Rodrigues, V. Lakshmi Nag, V. Tak, V. Venkatesh, C. Mukhopadhyay, V. Deotale, K. Padmaja, C. Wattal, S. Bhattacharya, T. Karuna, B. Behera, S. Singh, R. Nath, R. Ray, S. Baveja, B. A. Fomda, K. Sulochana Devi, P. Das, N. Khandelwal, P. Verma, P. Bhattacharyya, R. Gaind, L. Kapoor, N. Gupta, A. Sharma, D. VanderEnde, V. Siromany, K. Laserson, R. Guleria, R. Malhotra, O. Katoch, S. Katyal, S. Khurana, S. Kumar, R. Agrawal, K. Dev Soni, S. Sagar, N. Wig, P. Garg, A. Kapil, R. Lodha, M. Sahu, M. C. Misra, M. Lamba, S. Jain, H. Paul, J. Sarojini Michael, P. Kumar Bhatia, K. Singh, N. Gupta, D. Khera, D. Himanshu, S. Verma, P. Gupta, M. Kumar, M. Pervez Khan, S. Gupta, V. Kalwaje Eshwara, M. Varma, R. Attal, S. Sudhaharan, N. Goel, S. Saigal, S. Khadanga, A. Gupta, M. A. Thirunarayan, N. Sethuraman, U. Roy, H. Jyoti Raj, D. D'Souza, M. Chandy, S. Mukherjee, M. Kumar Roy, G. Goel, S. Tripathy, S. Misra, A. Dey, T. Misra, R. Ranjan Das, G. Bashir, S. Nazir, K. Ranjana Devi, L. Chaoba Singh, A. Bhargava, U. Gaikwad, G. Vaghela, T. Sukharamwala, A. Ch. Phukan, C. Lyngdoh, R. Saksena, R. Sharma, A. Velayudhan, Lancet Glob Health* ***2022****, 10, e1317, DOI: 10.1016/S2214-109X(22)00274-1.*

[12] *M. V. Murhekar, C. G. Kumar, Lancet Glob Health* ***2022****, 10, e1222, DOI: 10.1016/S2214-109X(22)00317-5.*

[13] *A. Mehta, V. D. Rosenthal, Y. Mehta, M. Chakravarthy, S. K. Todi, N. Sen, S. Sahu, R. Gopinath, C. Rodrigues, P. Kapoor, V. Jawali, P. Chakraborty, J. P. Raj, D. Bindhani, N. Ravindra, A. Hegde, M. Pawar, N. Venkatachalam, S. Chatterjee, N. Trehan, T. Singhal, N. Damani, Journal of Hospital Infection* ***2007****, 67, 168, DOI: 10.1016/j.jhin.2007.07.008.*

[14] *R. Lohiya, V. Deotale, GMS Hyg Infect Control* ***2023****, 18, Doc28, DOI: 10.3205/DGKH000454.*

[15] *Y. Karuppiah, Apollo Medicine* ***2024****, DOI: 10.1177/09760016241262582.*

[16] *M. A. Rather, K. Gupta, P. Bardhan, M. Borah, A. Sarkar, K. S. H. Eldiehy, S. Bhuyan, M. Mandal, J Basic Microbiol* ***2021****, 61, 380, DOI: 10.1002/JOBM.202000678.*

[17] *N. Bouhrour, P. H. Nibbering, F. Bendali, Pathogens* ***2024****, 13, 393, DOI: 10.3390/PATHOGENS13050393.*

[18] *A. Mishra, A. Aggarwal, F. Khan, Antibiotics* ***2024****, 13, 623, DOI: 10.3390/ANTIBIOTICS13070623.*

[19] *M. K. Pal, M. Lavanya, J Bio Tribocorros* ***2022****, 8, 1, DOI: 10.1007/S40735-022-00677-X/METRICS.*

[20] *E. Zhang, X. Zhao, J. Hu, R. Wang, S. Fu, G. Qin, Bioact Mater* ***2021****, 6, 2569, DOI: 10.1016/J.BIOACTMAT.2021.01.030.*

[21] *S. Kumar, D. N. Roy, V. Dey, Colloid Interface Sci Commun* ***2021****, 43, 100464, DOI: 10.1016/J.COLCOM.2021.100464.*

[22] *M. M. Tunney, S. P. Gorman, S. Patrick, Drugs* ***2012****, 65, 179, DOI: 10.2165/00003495-200565020-00003.*

[23] *A. D. S, S. P. A. P, J. Naveen, T. Khan, S. H. Khahro, Front Bioeng Biotechnol* ***2024****, 12, 1400918, DOI: 10.3389/FBIOE.2024.1400918/BIBTEX.*

[24] *L. Liu, X. Wu, Q. Wang, Z. Yan, X. Wen, J. Tang, X. Li, Corrosion Reviews* ***2022****, 40, 103, DOI: 10.1515/CORRREV-2021-0039/MACHINEREADABLECITATION/RIS.*

[25] *J. Knisz, R. Eckert, L. M. Gieg, A. Koerdt, J. S. Lee, E. R. Silva, T. L. Skovhus, B. A. An Stepec, S. A. Wade, FEMS Microbiol Rev* ***2023****, 47, 1, DOI: 10.1093/FEMSRE/FUAD041.*

[26] *N. Eliaz, Materials* ***2019****, 12, 407, DOI: 10.3390/MA12030407.*

[27] *S. Pandit, K. Gaska, R. Kádár, I. Mijakovic, ChemPhysChem* ***2021****, 22, 250, DOI: 10.1002/CPHC.202000769.*

[28] *K. K. A. Mosas, A. R. Chandrasekar, A. Dasan, A. Pakseresht, D. Galusek, Gels* ***2022****, 8, 323, DOI: 10.3390/GELS8050323.*

[29] *National Agency for Food & Drug Administration & Control, Drug Evaluation & Research (DER) Directorate, 'NAFDAC GOOD MANUFACTURING PRACTICE FOR MEDICAL DEVICES, IVDs, AND RELATED PRODUCTS GUIDELINES 2024',* ***2024****.*

[30] *Aluminium Alloy - Commercial Alloy - 1050A H14 Sheet, https://www.aalco.co.uk/datasheets/Aluminium-Alloy-1050A-H14-Sheet_57.ashx, accessed May 5,* ***2025****.*

[31] *Y. Y. Avcu, B. Gönül, O. Yetik, F. Sönmez, A. Cengiz, M. Guney, E. Avcu, Materials* ***2021****, 14, 6575, DOI: 10.3390/MA14216575.*

[32] *M. Witkowska, G. E. Thompson, T. Hashimoto, E. Koroleva, Surface and Interface Analysis* ***2013****, 45, 1585, DOI: 10.1002/SIA.5271.*

[33] *Aluminium: Corrosion, https://www.alumeco.com/aluminium/corrosion-of-aluminium/?s=0, accessed May 5,* ***2025****.*

[34] *J. S. de Andrade, M. R. S. Vieira, S. H. Oliveira, S. K. de Melo Santos, S. L. Urtiga Filho, Mater Chem Phys* ***2020****, 241, 122296, DOI: 10.1016/J.MATCHEMPHYS.2019.122296.*

[35] *J. Sahoo, S. Sarkhel, N. Mukherjee, A. Jaiswal, ACS Omega* ***2022****, 7, 45962, DOI: 10.1021/ACSOMEGA.2C06211.*

[36] *S. S. Nasker, P. M. Ajayan, S. Nayak, ACS Mater Lett* ***2023****, 5, 673, DOI: 10.1021/ACSMATERIALSLETT.2C01116.*

[37] *M. A. Islam, A. Hossain, N. Hossain, M. M. S. Ahmed, S. Islam, A. M. A. Henaish, A. V. Soldatov, M. A. Chowdhury, Sensors International* ***2024****, 5, 100293, DOI: 10.1016/J.SINTL.2024.100293.*

[38] *R. Podila, T. Moore, F. Alexis, A. Rao, J Vis Exp* ***2013****, e50276, DOI: 10.3791/50276.*

[39] *A. D. Staneva, D. K. Dimitrov, D. N. Gospodinova, T. G. Vladkova, Microorganisms 2021, Vol. 9, Page 1839* ***2021****, 9, 1839, DOI: 10.3390/MICROORGANISMS9091839.*

[40] *S. Bhatt, R. Pathak, V. D. Punetha, M. Punetha, J Mater Sci* ***2023****, 58, 7839, DOI: 10.1007/S10853-023-08534-Z.*

[41] *B. Polai, A. Samal, S. Ratha, D. Das, S. Kumar Nayak, Nano Express* ***2025****, 6, 015024, DOI: 10.1088/2632-959X/ADC31E.*

[42] *H. Huang, H. Guo, J. Qu, al -, Y. Cho, H. Lee, Y. Jeong, Z. Duan, in 'IOP Conference Series: Materials Science and Engineering', Vol. 493, IOP Publishing,* ***2019****, p. 012020, DOI: 10.1088/1757-899X/493/1/012020.*

[43] *J. Liu, Y. Wu, F. Yan, Y. Yan, F. Wang, G. Zhang, L. Zeng, Y. Ma, J. Guo, Y. Li, P. Zhang, Prog Org Coat* ***2025****, 200, 108966, DOI: 10.1016/J.PORGCOAT.2024.108966.*

[44] *D. K. Ojha, B. Polai, S. S. Nasker, A. Mehra, S. R. Das, S. K. Nayak, P. M. Ajayan, S. Nayak, Adv Mater Interfaces* ***2025****, 12, 2400637, DOI: 10.1002/ADMI.202400637.*

[45] *X. Wu, L. Lian, S. Yang, G. He, J Mater Chem C Mater* ***2016****, 4, 8528, DOI: 10.1039/C6TC02424F.*

[46] *S. Bittolo Bon, L. Valentini, J. M. Kenny, Chem Phys Lett* ***2010****, 494, 264, DOI: 10.1016/J.CPLETT.2010.06.024.*

[47] *S. H. Ko, S. W. Kim, S. H. Lee, Y. J. Lee, Sci Rep* ***2023****, 13, 1, DOI: 10.1038/s41598-023-47693-6.*

[48] *B. P. Singh, B. K. Jena, S. Bhattacharjee, L. Besra, Surf Coat Technol* ***2013****, 232, 475, DOI: 10.1016/J.SURFCOAT.2013.06.004.*

[49] *ASTM G1-03, Standard Practice for Preparing, Cleaning, and Evaluating Corrosion Test Specimens, ASTM International, https://store.astm.org/g0001-03r17e01.html, accessed May 5,* ***2025****.*

[50] *S. Panda, T. K. Rout, A. D. Prusty, P. M. Ajayan, S. Nayak, Advanced Materials* ***2018****, 30, 1702149, DOI: 10.1002/ADMA.201702149.*

[51] *J. Kim, W. H. Khoh, B. H. Wee, J. D. Hong, RSC Adv* ***2015****, 5, 9904, DOI: 10.1039/C4RA12980F.*

[52] *J. Horkstra, L. J. Van Der Pauw, N. V. Philips, Journal of Electronics and Control* ***1959****, 7, 169, DOI: 10.1080/00207215908937197.*

[53] *I. Y. Konyashin, T. V. Chukalovskaya, Surf Coat Technol* ***1997****, 88, 5, DOI: 10.1016/S0257-8972(95)02758-0.*

[54] *F. C. Walsh, C. Ponce de León, C. Kerr, S. Court, B. D. Barker, Surf Coat Technol* ***2008****, 202, 5092, DOI: 10.1016/J.SURFCOAT.2008.05.008.*

[55] *S. H. Ahn, J. H. Lee, H. G. Kim, J. G. Kim, Appl Surf Sci* ***2004****, 233, 105, DOI: 10.1016/J.APSUSC.2004.03.213.*

[56] *J. Creus, H. Mazille, H. Idrissi, Surf Coat Technol* ***2000****, 130, 224, DOI: 10.1016/S0257-8972(99)00659-3.*

[57] *M. Leonhard, B. Zatorska, D. Moser, B. Schneider-Stickler, Biomed Res Int* ***2019****, 2019, 8051270, DOI: 10.1155/2019/8051270.*

[58] *A. Kumar, P. K. Vemula, P. M. Ajayan, G. John, Nat Mater* ***2008****, 7, 236, DOI: 10.1038/NMAT2099.*

[59] *J. R. Pringle, Methods Enzymol* ***1991****, 194, 732, DOI: 10.1016/0076-6879(91)94055-H.*

[60] *X. Wang, J. Bing, Q. Zheng, F. Zhang, J. Liu, H. Yue, L. Tao, H. Du, Y. Wang, H. Wang, G. Huang, Emerg Microbes Infect* ***2018****, 7, DOI: 10.1038/S41426-018-0095-0.*

[61] *H. Yue, J. Bing, Q. Zheng, Y. Zhang, T. Hu, H. Du, H. Wang, G. Huang, Emerg Microbes Infect* ***2018****, 7, DOI: 10.1038/S41426-018-0187-X.*

[62] *S. Sharma, J. Acharya, M. R. Banjara, P. Ghimire, A. Singh, BMC Res Notes* ***2020****, 13, 1, DOI: 10.1186/S13104-020-4895-7.*

[63] *P. Fazii, E. Ciancaglini, G. Riario Sforza, European Journal of Clinical Microbiology and Infectious Diseases* ***2002****, 21, 373, DOI: 10.1007/S10096-002-0731-3/METRICS.*

[64] *E. F. Haney, M. J. Trimble, R. E. W. Hancock, Nature Protocols 2021 16:5* ***2021****, 16, 2615, DOI: 10.1038/s41596-021-00515-3.*

[65] *M. P. Murphy, H. Bayir, V. Belousov, C. J. Chang, K. J. A. Davies, M. J. Davies, T. P. Dick, T. Finkel, H. J. Forman, Y. Janssen-Heininger, D. Gems, V. E. Kagan, B. Kalyanaraman, N. G. Larsson, G. L. Milne, T. Nyström, H. E. Poulsen, R. Radi, H. Van Remmen, P. T. Schumacker, P. J. Thornalley, S. Toyokuni, C. C. Winterbourn, H. Yin, B. Halliwell, Nat Metab* ***2022****, 4, 651, DOI: 10.1038/S42255-022-00591-Z.*

[66] *P. C. Liao, E. J. Yang, L. A. Pon, STAR Protoc* ***2020****, 1, 100160, DOI: 10.1016/J.XPRO.2020.100160.*

[67] *NACE Standard RP0775-2005 - Preparation, Installation, Analysis, and Interpretation of Corrosion Coupons in Oilfield Operations, https://webstore.ansi.org/standards/nace/nacestandardrp07752005?srsltid=AfmBOoo EwMuikXp0sU7qJ4f-5ow1Xs9P2pAvyH7yQjONhMQ4syB9C5-y, accessed May 5,* ***2025****.*

[68] *J. Grossenbacher, M. R. Gullo, F. Dalcanale, G. Blugan, J. Kuebler, S. Lecaudé, H. Tevaearai Stahel, J. Brugger, J Biomed Mater Res A* ***2015****, 103, 3625, DOI: 10.1002/JBM.A.35477.*

[69] *K. Lim, R. R. Y. Chua, B. Ho, P. A. Tambyah, K. Hadinoto, S. S. J. Leong, Acta Biomater* ***2015****, 15, 127, DOI: 10.1016/J.ACTBIO.2014.12.015.*

[70] *B. S. Necula, J. P. T. M. Van Leeuwen, L. E. Fratila-Apachitei, S. A. J. Zaat, I. Apachitei, J. Duszczyk, Acta Biomater* ***2012****, 8, 4191, DOI: 10.1016/J.ACTBIO.2012.07.005.*

[71] *G. K. Das, P. P. Y. Chan, A. Teo, J. S. C. Loo, J. M. Anderson, T. T. Y. Tan, J Biomed Mater Res A* ***2010****, 93, 337, DOI: 10.1002/JBM.A.32533.*

[72] *X. Liu, K. Shan, X. Shao, X. Shi, Y. He, Z. Liu, J. A. Jacob, L. Deng, Int J Nanomedicine* ***2021****, 16, 753, DOI: 10.2147/IJN.S289008.*

[73] *ISO 10993-5:2009 - Biological evaluation of medical devices — Part 5: Tests for in vitro cytotoxicity, https://www.iso.org/standard/36406.html, accessed May 5,* ***2025****.*

[74] *L. Liu, D. Mandler, Electrochem commun* ***2020****, 120, 106830, DOI: 10.1016/J.ELECOM.2020.106830.*

[75] *J. Bin Wu, M. L. Lin, X. Cong, H. N. Liu, P. H. Tan, Chem Soc Rev* ***2018****, 47, 1822, DOI: 10.1039/C6CS00915H.*

[76] *S.-G. Kim, O.-K. Park, J. H. Lee, B.-C. Ku, Carbon letters* ***2013****, 14, 247, DOI: 10.5714/CL.2013.14.4.247.*

[77] *M. Kong, M. Garriga, J. S. Reparaz, M. I. Alonso, ACS Omega* ***2022****, 7, 39429, DOI: 10.1021/ACSOMEGA.2C05945.*

[78] *S. H. Chang, C. H. Chiang, F. S. Kao, C. L. Tien, C. G. Wu, IEEE Photonics J* ***2014****, 6, DOI: 10.1109/JPHOT.2014.2331254.*

[79] *Y. Raghupathy, A. Kamboj, M. Y. Rekha, N. P. Narasimha Rao, C. Srivastava, Thin Solid Films* ***2017****, 636, 107, DOI: 10.1016/J.TSF.2017.05.042.*

[80] *X. He, W. Zhou, Sci Rep* ***2024****, 14, 1, DOI: 10.1038/S41598-024-71736-1.*

[81] *S. Amiri, Silicon* ***2025****, 1, DOI: 10.1007/S12633-025-03298-4.*

[82] *M. Lipińska, P. Bazarnik, M. Lewandowska, Archives of Civil and Mechanical Engineering* ***2016****, 16, 717, DOI: 10.1016/j.acme.2016.04.013.*

[83] *R. Zhou, J. D. Embury, J. T. Wood, J. L. Smith, Mater Charact* ***1996****, 37, 239, DOI: 10.1016/S1044-5803(96)00179-9.*

[84] *S. Raygan, H. E. Mofrad, M. Pourabdoli, F. K. Ahadi, J Mater Process Technol* ***2011****, 211, 1810, DOI: 10.1016/J.JMATPROTEC.2011.06.002.*

[85] *D. B. Hani, R. Al Athamneh, Z. Albataineh, M. Rawashdeh, I. Makableh, Crystals (Basel)* ***2022****, 12, 457, DOI: 10.3390/CRYST12040457.*

[86] *C. H. Lin, W. T. Yeh, C. H. Chan, C. C. Lin, Nanoscale Res Lett **2012**, 7, 1, DOI: 10.1186/1556-276X-7-343.*

[87] *S. J. An, Y. Zhu, S. H. Lee, M. D. Stoller, T. Emilsson, S. Park, A. Velamakanni, J. An, R. S. Ruoff, Journal of Physical Chemistry Letters **2010**, 1, 1259, DOI: 10.1021/JZ100080C.*

[88] *N. Yadav, A. Dubey, S. Shukla, C. P. Saini, G. Gupta, R. Priyadarshini, B. Lochab, ACS Omega **2017**, 2, 3070, DOI: 10.1021/ACSOMEGA.7B00371.*

[89] *X. Zou, L. Zhang, Z. Wang, Y. Luo, J Am Chem Soc **2016**, 138, 2064, DOI: 10.1021/JACS.5B11411.*

[90] *S. I. Saeed, L. Vivian, C. W. S. C. W. Zalati, N. I. M. Sani, E. Aklilu, M. Mohamad, A. A. M. Noor, K. Muthoosamy, N. F. Kamaruzzaman, BMC Vet Res **2023**, 19, 1, DOI: 10.1186/S12917-022-03560-6.*

[91] *S. Sharma, J. Mohler, S. D. Mahajan, S. A. Schwartz, L. Bruggemann, R. Aalinkeel, Microorganisms **2023**, 11, 1614, DOI: 10.3390/MICROORGANISMS11061614.*

[92] *Y. Zhou, H. Wang, C. Zhang, Q. Zhou, D. F. Rodrigues, Front Mater **2022**, 9, 910152, DOI: 10.3389/FMATS.2022.910152.*

[93] *G. Cao, J. Yan, X. Ning, Q. Zhang, Q. Wu, L. Bi, Y. Zhang, Y. Han, J. Guo, Colloids Surf B Biointerfaces **2021**, 200, 111588, DOI: 10.1016/J.COLSURFB.2021.111588.*

[94] *P. Zhang, Z. Guo, C. Chen, I. Lynch, Nano Today **2022**, 43, 101436, DOI: 10.1016/J.NANTOD.2022.101436.*

[95] *C. Martini, F. Longo, R. Castagnola, L. Marigo, N. M. Grande, M. Cordaro, M. Cacaci, M. Papi, V. Palmieri, F. Bugli, M. Sanguinetti, Antibiotics **2020**, 9, 692, DOI: 10.3390/ANTIBIOTICS9100692.*

[96] *A. Krasowska, K. Sigler, Front Cell Infect Microbiol **2014**, 4, 102373, DOI: 10.3389/FCIMB.2014.00112.*

[97] *A. Kessler, J. Hedberg, E. Blomberg, I. Odnevall, Nanomaterials **2022**, 12, 1922, DOI: 10.3390/NANO12111922.*

[98] *J. J. Morris, A. L. Rose, Z. Lu, Redox Biol **2022**, 52, 102285, DOI: 10.1016/J.REDOX.2022.102285.*

[99] *A. Wojtala, M. Bonora, D. Malinska, P. Pinton, J. Duszynski, M. R. Wieckowski, Methods Enzymol **2014**, 542, 243, DOI: 10.1016/B978-0-12-416618-9.00013-3.*

[100] *G. E. Villalpando-Rodriguez, S. B. Gibson, Oxid Med Cell Longev **2021**, 2021, 9912436, DOI: 10.1155/2021/9912436.*

[101] *M. Yousefi, M. Dadashpour, M. Hejazi, M. Hasanzadeh, B. Behnam, M. de la Guardia, N. Shadjou, A. Mokhtarzadeh, Materials Science and Engineering: C **2017**, 74, 568, DOI: 10.1016/J.MSEC.2016.12.125.*

[102] G. Pizzino, N. Irrera, M. Cucinotta, G. Pallio, F. Mannino, V. Arcoraci, F. Squadrito, D. Altavilla, A. Bitto, Oxid Med Cell Longev **2017**, 2017, 8416763, DOI: 10.1155/2017/8416763.

[103] S. K. Pramanik, M. Bhuiyan, D. Robert, R. Roychand, L. Gao, I. Cole, B. K. Pramanik, Science of The Total Environment **2024**, 921, 171231, DOI: 10.1016/J.SCITOTENV.2024.171231.

[104] S. A. Park, J. G. Kim, Y. S. He, K. S. Shin, J. B. Yoon, Physics of Metals and Metallography **2014**, 115, 1285, DOI: 10.1134/S0031918X14130201.

[105] Y. Li, D. Xu, C. Chen, X. Li, R. Jia, D. Zhang, W. Sand, F. Wang, T. Gu, J Mater Sci Technol **2018**, 34, 1713, DOI: 10.1016/J.JMST.2018.02.023.

[106] C. Ejileugha, K. M. Ezealisiji, A. N. Ezejiofor, O. E. Orisakwe, J Bio Tribocorros **2021**, 7, 1, DOI: 10.1007/S40735-021-00545-0.

[107] R. Zuo, Appl Microbiol Biotechnol **2007**, 76, 1245, DOI: 10.1007/S00253-007-1130-6.

[108] I. Khosravi, Z. Shahryari, S. M. Jazaeri Moghadas, M. Yeganeh, H. T. Sarraf, Corrosion Protection at the Nanoscale **2020**, 127, DOI: 10.1016/B978-0-12-819359-4.00008-8.

[109] Y. Guo, Z. Xu, Q. Wang, S. Zu, M. Liu, Z. Yu, Z. Zhang, L. Ren, Prog Org Coat **2022**, 164, 106722, DOI: 10.1016/J.PORGCOAT.2022.106722.

[110] M. I. Necolau, A. M. Pandele, Coatings **2020**, 10, 1149, DOI: 10.3390/COATINGS10121149.

[111] S. J. Richard Prabakar, Y. H. Hwang, E. G. Bae, D. K. Lee, M. Pyo, Carbon N Y **2013**, 52, 128, DOI: 10.1016/J.CARBON.2012.09.013.

[112] T. Mosmann, J Immunol Methods **1983**, 65, 55, DOI: 10.1016/0022-1759(83)90303-4.

[113] I. Koyuncu, A. Gönel, A. Akdağ, M. A. Yilmaz, Cell Mol Biol **2018**, 64, 75, DOI: 10.14715/CMB/2018.64.1.14.

[114] S. Gurunathan, M. A. Iqbal, M. Qasim, C. H. Park, H. Yoo, J. H. Hwang, S. J. Uhm, H. Song, C. Park, J. T. Do, Y. Choi, J. H. Kim, K. Hong, Nanomaterials **2019**, 9, 969, DOI: 10.3390/NANO9070969.

[115] M. R. Rahimzadeh, M. R. Rahimzadeh, S. Kazemi, R. J. Amiri, M. Pirzadeh, A. A. Moghadamnia, Emerg Med Int **2022**, 2022, 1480553, DOI: 10.1155/2022/1480553.

[116] C. Exley, Environ Sci Process Impacts **2013**, 15, 1807, DOI: 10.1039/C3EM00374D.

[117] K. Catt, H. Li, X. T. Cui, Acta Biomater **2017**, 48, 530, DOI: 10.1016/J.ACTBIO.2016.11.039.

[118] V. Srimaneepong, D. Rokaya, P. Thunyakitpisal, J. Qin, K. Saengkiettiyut, Sci Rep **2020**, 10, 1, DOI: 10.1038/s41598-020-60070-x.

[119] *S. P. Cangui-Panchi, A. L. Ñacato-Toapanta, L. J. Enríquez-Martínez, J. Reyes, D. Garzon-Chavez, A. Machado, Curr Res Microb Sci* ***2022****, 3, 100175, DOI: 10.1016/J.CRMICR.2022.100175.*